

# Precipitation projections using a spatiotemporal distributed method: a case study in the Poyang Lake Watershed based on MRI-CGCM3

Ling Zhang<sup>1</sup>, Xiaoling Chen<sup>1,2</sup>, Jianzhong Lu<sup>1,\*</sup>, Dong Liang<sup>1</sup>

<sup>1</sup>State Key Laboratory of Information Engineering in Surveying, Mapping and Remote Sensing, Wuhan University, Wuhan 430079, China

<sup>2</sup>Key Laboratory of Poyang Lake Wetland and Watershed Research, Ministry of Education, Jiangxi Normal University, Nanchang 330022, China

\* *Correspondence to:* Jianzhong Lu (lujzhong@whu.edu.cn)

**Abstract.** To bridge the gap between large-scale GCM (Global Climate Model) outputs and regional-scale climate requirements of hydrological models, a spatiotemporally distributed downscaling model (STDDM) was developed. The STDDM was done in three stage: (1) upsampling grid-observations and GCM (Global Climate Model) simulations to spatially continuous finer-grids; (2) creating the mapping relationship between the observations and the simulations, differently in space and time; (3) correcting the simulation and produced downscaled data in spatially continuous grid scale. We applied the STDDM to precipitation downscaling in Poyang Lake Watershed using MRI-CGCM3 (Meteorological Research Institute Coupled Ocean-Atmosphere General Circulation Model3), with an accepted uncertainty of  $\leq 4.9\%$ ; then created future precipitation changes from 1998 to 2100 (1998-2012 in the historical and 2013-2100 in the RCP8.5 scenario). The precipitation changes increased heterogeneities in temporal and spatial distribution under future climate warming. In terms of temporal patterns, the wet season become wetter while the dry season become drier. The frequency of extreme precipitation increased while that of the moderate precipitation decreased. Total precipitation increased while rain days decreased. The max continuous dry days and the max daily precipitation both increased. In terms of spatial patterns, the dry area exhibited a drier condition during the dry season; the wet area exhibited a wetter condition during the wet season. Analysis with temperature increment showed precipitation changes can be significantly explained by climate warming, with  $p < 0.05$  and  $R \geq 0.56$ . The precipitation changes and explains indicated the downscaling method is reasonable and the STDDM could be applied in the basin-scale region based on a GCM successfully. The results implicated an increasing risk of flood-droughts under global warming, which were a reference for water balance analysis and water resource planting.

## 26 **1 Introduction**

27 Global warming has caused temporal and spatial redistributions of precipitation (Frei et al. 1998; Trenberth et al. 2011) and  
28 has increased the frequency and intensity of floods and droughts, seriously threatening social systems and ecosystems (Pall et al,  
29 2000; Dai, 2013). To the fragile ecological and living environments, what the future hydrological situation will be under future  
30 global warming is a crucial question to avoid or reduce damages from climate warming.

31 Global Climate Models (GCMs) are basic tools for assessing the effects of future climate change and provide an initial source  
32 for future climates (Xu, 1999). However, GCMs have coarse global resolutions ranging from  $1^{\circ}\times 1^{\circ}$  to  $4^{\circ}\times 4^{\circ}$ , and are not  
33 applicable in regional scales, such as watersheds. Downscaling algorithms have been developed to link the global-scale GCM  
34 outputs and the regional-scale climate variables, including dynamic (Giorgi, 1990; Teutschbein and Seibert, 2012) and statistic  
35 (Wilby et al., 2007; Chu et al., 2010) models. The dynamic method employs regional climate models (RCMs) that are nested  
36 inside GCMs based on the complex physics of atmospheric processes and involves high computational costs. Limited by an  
37 insufficient understanding of the physical mechanism and expensively computing resources, the dynamic downscaling model  
38 cannot easily satisfy small and mid-size region as the Poyang Lake Watershed. Unlike dynamic downscaling, statistic  
39 downscaling constructs an empirical relationship between climate variables of the global-scale and local-scale, with  
40 inexpensive computations. Benefiting from inexpensive computations and easy implementations, downscaling methods have  
41 been widely used, including regression models (Labraga et al. 2010, Quintana et al. 2010; Zorita et al. 1999), weather typing  
42 schemes (Boéj et al. 2007; ENKE et al. 2005) and weather generators (Mullan et al., 2016; Baigorria and Jones et al., 2011).  
43 Most statistical downscaling methods are conducted on discrete stations (Charles et al., 1999; Zhang et al., 2005; Maurer et  
44 al., 2008; Mullan et al., 2016; Alaya et al., 2017; Chen et al., 2018) and produce downscaled data the in the station scale.,  
45 including single-station and multi-station methods. The single-station method produces the downscaled climate variable at a  
46 single point (or watershed average), or independently at several points (Zhang et al., 2005; Maurer et al., 2008). The multi-  
47 station method generates the downscaled climate variable dependently for multiple sites (Charles et al., 1999; Alaya et al.,  
48 2017; Chen et al., 2018). For both the single-station and multi-station methods, the specific downscaling relationship and  
49 downscaled climate variable are both discrete in the station scale, instead of being spatially continuous in a grid-scale of a

50 finer-resolution. Compared to the spatially continuous grid data, discrete stations are sparse. As underlays of local region are  
51 complex with different topographies, land covers, and clouds coverage, the discrete point-scale data underrepresents the spatial  
52 variability. For ungauged areas without station coverage, it is inviable to obtain high-quality downscaling relationships and  
53 downscaled local climate variables. Moreover, compared to point-scale data, spatially continuous grid data can express the  
54 spatial distribution of climate variables more accurately and clearly; thus express the spatial correlation and heterogeneity  
55 more accurately and clearly. Additionally, spatially continuous grid data can be directly used in a spatially distributed or semi-  
56 distributed hydrological model, such as Crest (Wang et al., 2011), VIC (Lohmann et al. 1998), and MIKE SHE (DHI, 2014),  
57 which is the forefront of international hydrological scientific research (Beven et al. 1990). Spatially continuous downscaled  
58 climate data can also be easily integrated with remote sensing data of geologies, topographies, soils, or land covers. In fact,  
59 spatially continuous data is widely used in the rapidly developing field of remote sensing, which benefits hydrological models  
60 by providing a data source (Engman et al., 1991). Therefore, the downscaling method processed on spatially continuous data  
61 is of vital importance.

62 Some downscaling methods could obtain spatially continuous data. Dynamic downscaling methods could produce downscaled  
63 climate variables in spatial continuous grid-scale. However, the downscaled grid-data is commonly limited in the resolution,  
64 coarser than 25 kilometers (Trzaska et al., 2014; Maraun et al, 2010); thus could not be applied to small watersheds. A few  
65 statistical downscaling methods of the weather generator could provide downscaled climate variables in a spatially continuous  
66 scale (Perica et, al., 1996; Venema et al., 2010). The specific algorithms can be divided into three cartographies: transformed  
67 Gaussian processes (Guillot and Lebel, 1999), point process models (Wheater et al., 2005; Cowpertwait et al., 2002), and  
68 spatial-temporal implementation of multifractal cascade models (Lovejoy and Schertzer, 2006). However, few researches have  
69 implicated these approaches on GCM outputs. Furthermore, as the refined data obtain from the weather generator is biased  
70 from the observed data, correction is needed. However, in the researches, there is no observed field of finer-resolution  
71 corresponding to the downscaled scale; thus, not all the spatial unit in the downscaled field could be corrected by the observed  
72 field.

73 As the factors driving climate variables vary in regions and seasons, the statistical downscaling method should consider the  
74 spatial and temporal heterogeneity (Fowler et al., 2007; Manzanas et al., 2018). Most methods (Charles et al., 1999; Maurer et

75 al., 2008; Alaya et al., 2017) performed the downscaling for each specific-site (or specific type sites), respectively; thus the  
76 downscaled result showed spatial heterogeneity. However, few downscaling methods consider the spatial heterogeneity in a  
77 spatially continuous scale. In terms of temporal heterogeneity, some downscaling algorithms are processed independently on  
78 months (or seasons) (Boé et al., 2007; Leander and Buishand, 2007). For the different time, the algorithm or parameters are  
79 different; thus the temporal heterogeneity is expressed. However, few downscaling methods consider temporal heterogeneity  
80 combined with spatial heterogeneity in the spatially continuous scale.

81 To produce downscaled data in a spatially continuous scale and consider temporal heterogeneity combined with spatially  
82 continuous heterogeneity, the study proposed a spatiotemporally distributed downscaling method (STDDM). A finer-  
83 resolution observed field (Hutchinson et al., 1998a; Hutchinson et al., 1998b) is induced as the reference to correct the refined  
84 GCM outputs for each grid and time; subsequently, the corrected data is produced as the downscaled data. The correction is  
85 distributed in time and continuous-space.

86 The Poyang Lake Watershed is sensitive to climate changes in the East Asian monsoon region and therefore is not immune to  
87 global warming. Redistributions of precipitation due to global warming have resulted in an increased occurrence of extreme  
88 hydrological events, an enhanced flood frequency and intensity (Wang et al., 2009; Guo et al., 2006), a significant decline in  
89 lake level and inundation area (Feng et al. 2012; Zhang et al. 2014), which threatened to fragile wetland and forest ecosystems  
90 (Han et al. 2015, Dyderski et al. 2018), economic developments and human lives (Ye et al., 2011). However, the Poyang Lake  
91 Wetland ecosystem is an internationally important habitat for migratory birds, abundant of biodiversity and regarded as a  
92 Natural Reserve. In addition, the watershed is a commercial grain production area and an important part of the Yangtze River  
93 Economic Belt. As this region is economically and ecologically significant, investigating the future precipitation changes in  
94 the watershed is crucial for protection from climate damages. Previous studies of future precipitation changes in the Poyang  
95 Lake Watershed include temporal and special patterns. Precipitation changes in temporal pattern, focused on intensity and  
96 frequency of precipitation extremes (Hong et al. 2014; Wang et al. 2017), as well as the annual or quarterly total precipitation  
97 (Guo et al., 2010; Guo et al., 2008; Li et al., 2016). In spatial pattern, precipitation change analysis covers five subbasins  
98 (Xinjiang, Raohe, Xiushui, Ganjiang and Fuhe subbasins) (Guo, et al. 2010; Hong, et al. 2014) and 13 discrete meteorological  
99 stations (Li et al. 2016), or 7 coarse grids (Guo, et al. 2008). There has been little research concerning the spatial-temporal

100 distribution of precipitation in a continual fine-resolution grids space. In addition, driving force analysis of precipitation  
101 changes related to temperatures increment has not been conducted.

102 In the study, taking Poyang Lake Watershed as a test case, we projected future precipitations based on the spatiotemporally  
103 distributed downscaling method (STDDM), using MRI-GCM3 simulations and meteorological observations. The objects are  
104 as the following: (1) to develop a spatiotemporally distributed downscaling method (STDDM), projecting future climate  
105 variables in spatially continual scale; and (2) to document temporal and spatial changes in precipitation for the Poyang Lake  
106 Watershed in the 21st century and the correlations between these precipitation changes and temperature increment. Future  
107 precipitation changes can provide basic hydrological information necessary to a better understanding of water volumes and  
108 flood-droughts risks; furtherly benefits wetland and forest ecosystem conservation and aids decision-making in development,  
109 utilization, and planning of water resources.

## 110 **2 Study area and datasets**

### 111 **2.1 Study Area**

112 Poyang Lake Basin (24°28'-30°05' N and 113°33'-118°29'E) is located in the southeast of China, connected with Yangtze  
113 River in the north (Fig. 1). Within the southeast subtropical monsoon zone, the annual average temperature of the watershed  
114 is 17.5°C. The mean annual precipitation is 1638 mm, with 192 rainy days (daily precipitation  $\geq 0.1$  mm/day) and 173 rain-  
115 free days (daily precipitation  $< 0.1$  mm/day). The rainy season lasts from April to July, occupying about 70% of the annual  
116 total amount. Inter or intra annual precipitation variations are dominated by the southeast and southwest monsoon, mainly in  
117 summer. With a coverage area of 162000 km<sup>2</sup>, the diversities of topographies also effect on precipitation changes. The  
118 topography varies from high mountains of Luoxiao, Wuyi, and Nanling in east, south and west, with the elevation reaching to  
119 the 2200m, to the depressing of Ji Tai or Ganzhou Depressing in the south or center and alluvial plains of Poyang Lake Plain  
120 in the north, with the elevation reaching to  $< 50$  m (1a). The different topography and location generate the uneven distribution  
121 of precipitation in space and produce less rain in the depressing, plains, and hills area because of the leeward sloop, but more  
122 orographic rain in the mountain area for the reason of the windward sloop (1b) (Mingjin et al. 2011). To analyze precipitation

123 changes in the rich- or poor-rain area, the meteorological stations were classified into dry and wet stations (Fig. 1a and b),  
124 according to the annual precipitation amount. We sorted the annual precipitation averaged over the time from 1961 to 2005,  
125 of the 15 stations. The four stations with the max or min mean annual precipitations are set as dry or wet stations, indicating  
126 the dry or wet area (Fig.1b), respectively.

127 In the past 50 years of the Poyang Lake Watershed, annual mean temperature indeed experiences a significant ( $p < 0.02$ ) increase  
128 with a change rate of  $0.15\text{ }^{\circ}\text{C}/10\text{a}$  (Fig.1d), based on the meteorological observations from 1961 to 2005. Under the temperature  
129 increasing condition, the precipitation in temporal and spatial distribution becomes more uneven (Zhan et al. 2011), which  
130 increases the risk of floods and droughts (Li et al. 2016; Ye et al. 2011).

## 131 **2.2 Data sets**

132 Global Climate Models (GCMs) are widely used tools to project future climate change. GCMs from the Coupled Model  
133 Intercomparison Project Phase Five (CMIP5) performs better than other CMIPs such as CMIP3 and CMIP4, with generally  
134 finer resolution and more improved physical mechanism (Sperber, 2013; Taylor et al. 2012). Compared to the other CGMs of  
135 CMIP5, the MRI-CGCM3 (Meteorological Research Institute Coupled Ocean-Atmosphere General Circulation Model3,  
136 Yukimoto et al. 2012) performs better in simulating diurnal rainfall over subtropical China (Yuan et al. 2013) and has the  
137 finest resolution of  $1.121^{\circ} \times 1.125^{\circ}$ . Thus we select MRI-CGCM3 data applied in Poyang Lake Watershed to test the  
138 performance of the STDDM.

139 The future data of MRI-CGCM3 includes simulations of the Representative Concentration Pathways (RCPs) of 8.5,6, 4.5 and  
140 2.6. Compared to the other RCPs, in the RCP8.5 scenario temperature increases the most, which is corresponds to a highest  
141 greenhouse gas emission, leading to a radiative forcing of  $8.5\text{ W}/\text{m}^2$  and temperature increase of  $7.14\text{ }^{\circ}\text{C}$  at the end of 21st  
142 century (Taylor et al. 2012). The research is to detect the remarkable precipitation changes under climate warming; thus we  
143 selected future simulations in the RCP8.5 scenario. In the study, we merge the historical (from 1961 to 2005), historical extent  
144 (from 2006 to 2012) and RCP85 (from 2013 to 2100) data, as the merged data (1961-2100). To quantitatively analyze the  
145 precipitation changes under climate warming in the 21st century, we compared precipitation between the baseline and future  
146 period. As annual precipitation observations have main oscillation periods of quasi-20 years (Zhan et al. 2011), we selected

147 three 20 years from the merged data. From the merged data, simulations from 1998 to 2017 were selected as the baseline period  
148 data, simulations from 2041 to 2060 were selected as the near future period data, and simulations from 2081 to 2100 were  
149 selected as the further future period data.

150 The local grid observations (Hutchinson et al., 1998a; Hutchinson et al., 1998b; Zhao et al., 2014) with a resolution of  $0.5^{\circ} \times 0.5^{\circ}$   
151 are downloaded from the China Meteorological Data Service Center (<http://data.cma.cn/>). The local grid observations and  
152 MRI-CGCM3 historical simulations were used to construct a relationship to correct the GCM data. China metrology point data  
153 were also downscaled and used to validate the grid observations and the downscaled GCM simulations. To investigate the  
154 relationship between precipitation changes and the temperature increment, we extract not only precipitations but also  
155 temperature.

### 156 **3 Methodology**

#### 157 **3.1 Future climate projection based on the spatiotemporally distributed downscaling model**

158 Considering the spatiotemporal heterogeneity of precipitation at the regional scale such as the Poyang Lake Watershed, we  
159 developed a spatiotemporally distributed downscaling model (STDDM), which is a logical framework based on a specific  
160 mathematic algorithm. The mathematic algorithm was used to create a mapping relationship between the global-scale GCM  
161 simulations and the local scale climates variables. The mapping relationship is used as a transform function to correct the  
162 future climate simulations to no-bias data. In the framework, we constructed respective mapping relationships between the  
163 match-ups of GCMs simulations and local climate observations in each time (e.g., months or seasons) at each location. The  
164 STDDM was improved compared to the traditional downscaling methods by adjusting the specific downscaling algorithm to  
165 be suitable in the distributed space and time. Therefore, the downscaling processes show spatiotemporal differences in the  
166 parameters or the equations, and the output data are spatially continuous, unlike that in traditional downscaling methods, which  
167 ignores the temporal and continuous spatial differences and express space as discrete points instead of continuous grids.

168 Figure 2a shows the logical framework of the STDDM while Fig. 2b demonstrates how it was applied in Poyang Lake  
169 Watershed using MRI-CGCM3 based on a linear-scaling algorithm. The STDDM contains three parts (Fig. 2a and b): (1)

170 upsampling GCMs simulations and local-scale observations to a continuous grid space of the same finer resolution; (2)  
171 constructing respective mapping relationship between the GCMs simulations and local observations in distributed space and  
172 time; (3) correcting the GCMs simulations using the mapping relationship constructed in step 2.

### 173 **3.1.1 Upsampling GCMs simulations**

174 MRI-GCM3 simulations were interpolated by Natural Neighbor Interpolation (Sibson et al., 1981) to a scale of 20 km×20 km,  
175 the smallest size of the subbasin of the Poyang Lake Watershed (Zhang et al. 2017), generating 263 spatial grids (Fig. 2b). For  
176 the spatiotemporally distributed downscaling, we used China meteorology spatially continua grid data as observations, instead  
177 of China meteorology station data. We interpolated the gridded observations to 20 km × 20 km, the same as the downscaled  
178 climate simulations. The match-up grids of simulations and observations at each time and each grid-box were generated.

### 179 **3.1.2 Constructing relationships between the GCMs simulations and local observations**

180 Because there is an inevitable mismatch between the simulations and observations (Li, 2009; Wood et al., 2004) after the  
181 upsampling, bias correction should be performed. The bias correction was processed by the transform function between match-  
182 ups of the upsampled simulation and observations, which represents the mapping relationship between the match-ups. The  
183 transform function could be any bias corrected model, including linear scaling, local intensity scaling, power transformation,  
184 distribution mapping models (Teutschbein et al. 2012) and other linear or nonlinear regression models.

185 As the influencing factors on climates show heterogeneity in space and time, we created spatiotemporally distributed  
186 relationships, described by the following formula.

$$C'_{T,S} = F_{T,S}(C_{T,S}) \quad (1)$$

187 Where,  $C'_{T,S}$  and  $C_{T,S}$  indicate the upsampled global-scale climate simulations and the local climate variables, respectively,  
188 in the given time of  $T$  and the space of  $S$ .  $F_{T,S}$  demonstrates a transform function, used to correct the upsampled GCMs  
189 simulations. The function is a specific bias correction model, spatiotemporally distributed in mathematic equations or  
190 parameters, which is constructed based on the data from the historical period of 1961 to 2005.



191 In this study, we use a linear-scaling algorithm (Lenderink et al., 2007) as the bias correction model. For the linear-scaling  
192 algorithm, the simulations were corrected by the discrepancy between the simulations and observations. Precipitations derived  
193 from the GCMs were corrected by multiplying the precipitation bias coefficient, which is the ratio of the mean monthly  
194 observation to simulation from the historical period; temperatures were corrected by adding the temperature bias coefficient,  
195 which is the difference between the mean monthly observation and simulation in the historical period. However, as the bias  
196 varies among the months from January to December and among the locations of the 236 spatial grids, a global standard bias  
197 coefficient is prohibited. To better capture the bias in distributed time and space, we should create an individual bias coefficient  
198 for the given month and grid box. Thus, a spatiotemporally distributed bias matrix was constructed. The respective downscaling  
199 model and bias coefficient for a given month ( $T$ ) and space ( $S$ ) were established by Eq. 2 and 3.

$$P' = P \times P\_Cof \quad (2)$$

$$TM' = TM + TM\_Cof \quad (3)$$

200 where  $P(T)$  represents the precipitation (or temperature) of upsampled simulations.  $P'(TM')$  represents the downscaled result  
201 or upsampled observations;  $P\_Cof$  ( $TM\_Cof$ ) represents the bias correction coefficient of precipitations (or temperatures). In  
202 the construction of  $P\_Cof$  ( $TM\_Cof$ ),  $P(TM)$  and  $P'(TM')$  was set as the average monthly precipitation (or temperature) over  
203 the historical time from 1961 to 2005. All the input and output data in the equations are in the given month ( $T$ ) and space ( $S$ ).

### 204 **3.1.3 Correcting the GCMs simulations**

205 The constructed relationship between the GCMs simulations and the observations from the historical period (in section 3.1.2)  
206 also hold for the future (Maraun et al., 2010). Thus, the transform function was used to correct the future CGCMs simulations.  
207 In this study, we corrected the daily and monthly precipitations (or temperatures) from MRI-CGCM3 by adding (or multiplying)  
208 the bias coefficients in the corresponding month and grid box.

## 209 **3.2 Precipitation changes analysis**

### 210 **3.2.1 Statistic indexes of precipitation changes**

211 To obtain the general change in the temporal distribution, we calculated monthly precipitations from 1998 to 2100, averaged  
212 over the whole watershed. As floods and droughts occur more frequently in wet and dry months, we specifically analyze the  
213 extreme wet and dry precipitation changes in the 21st century. Therein, monthly precipitations, > 75% percentile of the 12  
214 months, were classified as the extreme wet monthly precipitations for each year of the 103 years; monthly precipitations, ≤  
215 25% percentile were classified as the extreme dry monthly precipitation. The monthly precipitation of the 25%-50% and 50%-  
216 75% quantiles were classified as normal dry and wet monthly precipitations. The wet monthly precipitations include extreme  
217 and normal wet monthly precipitations; the dry monthly precipitations include extreme and normal dry monthly precipitations.  
218 To understand precipitation dynamics in terms of frequency and intensity, daily precipitations were categorized into five  
219 classes based on the classification by the Chinese Meteorological Administration and the possible risk of floods and droughts:  
220 light rain, medium rain, heavy rain, rainstorm, and extreme rainstorm with daily precipitation of 0.1-10, 10-25, 25-50, 50-100  
221 and >100 mm/day, respectively. The frequency of precipitation intensities indicates heterogeneity in temporal distribution.  
222 The higher frequency of moderate rain means the more homogeneous, vice versa is the extreme rain. Therefore, the  
223 precipitation intensities were separated to moderate or extreme rains, including light rain, median rain or heavy rain, rainstorm,  
224 extreme rainstorm, respectively.

225 To further analyze the changes in precipitation frequencies and intensities, we calculate the annual days of light rain, medium  
226 rain, heavy rain, rainstorm and extreme rainstorm from 1998 to 2100 averaged over the whole watershed. Annual total  
227 precipitation, annual dry days, annual max daily precipitation and annual max continuous dry days were displayed as well.  
228 The meteorological stations (Fig. 1a) are uniformly distributed in the whole watershed and cover all kinds of the topographies  
229 and land covers. Therefore, in the study, the all above precipitation indexes of one year for the whole watershed were calculated  
230 based on the precipitation averaged over the grids containing the 15 stations, instead of the entire grids. Under global climate  
231 warming, precipitation becomes more concentrated which leads to more heterogeneity in temporal and spatial distribution  
232 (Donat et al., 2016; Min et al., 2011). Thus, we calculated variation coefficients for each year from 1998 to 2100, to investigate

233 the precipitation changes in temporal and spatial distribution. The variation coefficient measures the standard dispersion of the  
234 data items, which can indicate the unevenness of temporal and spatial distributions of the precipitation. In this study,  
235 heterogeneity in temporal, spatial and spatiotemporal distributions was measured by the temporal, spatial and spatiotemporal  
236 variation coefficient, respectively. Temporal variation coefficients were calculated on the daily or monthly precipitations in  
237 one year and the variation coefficient for one year is averaged over those of the 15 stations. For monthly precipitation, we only  
238 select extreme wet and dry precipitations, as the extreme wet and dry are more likely to cause floods or droughts and thus  
239 should be paid more attention. Spatial variation coefficients were calculated on the annual total precipitations of the 15 stations  
240 in one year. Spatiotemporal variation coefficient was calculated on the monthly precipitations of the extreme wet months of  
241 the wet stations and the extreme dry months of the dry stations in one year, as the extreme precipitation values were more  
242 likely to cause floods or droughts.

### 243 **3.2.2 Relationship analysis between precipitation changes and temperature increasing**

244 We investigated the precipitation changes as a result of global temperature increase. To this end, we made liner regression  
245 between the precipitation index and temperature changes from 2005 to 2100. We note that a mean filter with a window size of  
246 21 years can reduce potential random fluctuation from precipitation by the most; thus was used to smooth annual precipitation  
247 indexes and temperature simulations from 2005 to 2100. The long-time smoothed annual precipitation or temperature minus  
248 the average annual value from 1998 to 2017, are set as precipitation index or temperature changes. A linear regression model  
249 was used to investigate whether precipitation changes are related to climate warming. The two 11 years, 2005 to 2015 and  
250 2090 to 2100 at the start and end, did not have filter diameter of 21 years; thus climate data used to be regressed is from 2016  
251 to 2089.

## 252 **4 Result and Discussion**

### 253 **4.1 Model assessment**

254 Validation about the China meteorological grid observations should be performed, as well as the STDDM. As the STDDM  
255 introduce the China meteorological grid observations and the grid data is not the direct in-suit data, validation about the gridded

256 data is necessary. The determination coefficient ( $R^2$ ), root mean square error (RMSE) and PBias (percent bias) were used to  
257 examine the model performance.

#### 258 **4.1.1 Evaluation for the gridded meteorological**

259 The China meteorological grid observations are referenced data to corrected GCMs simulations and reliability of the  
260 observations is vital to the performance of the STDDM. So we make a validation using meteorological station observations,  
261 in Fig. 3.

262 As shown in Fig. 3, we select four meteorological stations. The selected stations are uniformly distributed. The validation  
263 produced an acceptable precision with  $R^2 > 0.91$ , absolute PBias  $< 2\%$  for precipitations and  $R^2 = 0.99$ , absolute PBias  $< 6\%$   
264 for temperature. All the dots of gridded and station value were distributed along the 1:1 line, thus confirming the satisfactory  
265 performance.

#### 266 **4.1.2 Validations of precipitation and temperature projections in Poyang Lake Watershed**

267 Before being used in future climate projection, the model should be examined. Data from 1961 to 1985 were used to construct  
268 the model, and the remaining historical data from 1986 to 2005 were used to validate.

269 To test whether the downscaling method (STDDM) is effective in climate projections, we compare the results before and after  
270 the bias correction in Fig. 4. The results before and after the bias correction marked as the outcomes by the STDDM and No-  
271 STDDM, respectively. The projections by the STDDM show better performance with high correlations and narrow bias,  
272 compared to the result by No-STDDM. Considering the complexity of climate physical mechanism and difficulty to accurately  
273 simulate by the present methods, the uncertainty could be acceptable.

274 Using the STDDM and MRI-CGCMs, we obtained the temporal and spatial variation of future precipitations in the Poyang  
275 Lake Watershed, and investigated the heterogeneity changes of precipitation in the temporal and spatial distribution.

#### 276 **4.2 Temporal variation of future precipitation**

277 To discover the temporal variation under the future climate warming, we analyzed the monthly and daily precipitation changes  
278 during the period from 1998 to 2100. For monthly precipitation, we analyzed intra-annual and inter-annual dynamics of

279 precipitation; based on the dynamics, we investigated the heterogeneity changes of monthly precipitation. For daily  
280 precipitation, we analyzed the changes of precipitation intensities and frequencies; based on the changes, heterogeneity  
281 changes of daily precipitation was also investigate.

#### 282 **4.2.1 Monthly precipitation changes**

283 We analyzed the monthly precipitation changes during the period from 1998 to 2100 in Fig. 5. Precipitation show significant  
284 intra-annual dynamics. Months with abundant rain (wet months), indicated by a reddish color, are mainly in April to July (the  
285 wet season), while the rain-poor months (dry months), indicated by a bluish color, are mainly in September to the subsequent  
286 February (the dry season). Precipitation concentrates in spring (March to May) and summer (July to August), occupying 73%  
287 of the annual amount. The intra-annual dynamics of precipitation is similar to that shown by Feng (2012). Precipitation also  
288 showed inter-annual dynamics. The wet months become wetter, and the wet season comes earlier from April to March, even  
289 in February. In addition, each monthly precipitations of seven months (April to November) took increasing trends, of which  
290 most months (5 months; April, May, June, August) are in the wet season; while precipitations of the other five months  
291 experienced decreasing trends, all of which were in the dry season. It seems that wet months become wetter and dry months  
292 become drier, in general.

293 To better demonstrate the inter-annual dynamics of precipitation, monthly precipitations in each year were sorted in a  
294 descending order in Fig. 5(b). As the time of the monsoon reaching the Poyang Lake Watershed, varied in different years, with  
295 1~2 months' advance or delay; the wet or dry months for different years are not the same. By sorting monthly precipitation,  
296 wet months and dry month could be distinguished intuitively in Fig. 5(b). Obviously, monthly precipitation of wet months  
297 experienced an increasing trend respectively, even some with slight significance; in contrast, each dry monthly precipitation  
298 exhibited decreasing trends, separately, despite the insignificant signs. We accumulated the extreme wet or dry monthly  
299 precipitations for each year in Fig. 6. The precipitation of extreme wet months showed a significantly increasing trend ( $p < 0.05$ )  
300 (Fig. 6a), while the precipitation of the extreme dry months demonstrated a significantly decreasing trend ( $p < 0.05$ ). Extreme  
301 wet months increased from  $277.82 \text{ mm} \cdot \text{month}^{-1}/\text{a}$  over historical time from 1998-2017, to  $344.10 \text{ mm} \cdot \text{month}^{-1}/\text{a}$  over future  
302 time from 2081 to 2100, by 23.86% with a change rate of  $7.3 \text{ mm} \cdot \text{month}^{-1}/10\text{a}$ . Extreme dry months decreased from  $35.44$

303 mm•month<sup>-1</sup>/a over historical time from 1998-2017, to 30.46 mm•month<sup>-1</sup>/a over future time from 2081 to 2100, by -14.05%  
304 with a change rate of 0.92 mm•month<sup>-1</sup>/10a. Therein, the extreme wet months are mainly concentrated in March-July (Fig. 6c),  
305 part of the wet season, while the extreme dry months are mainly concentrated in September-February (Fig. 6d), consistent to  
306 the dry season.

307 Overall, under climate warming over the 21st century, the wet monthly precipitations become wetter while the dry month  
308 precipitations become drier, which suggested the uneven temporal distribution of precipitation (Fig. 7). As shown in Fig. 7,  
309 the temporal variation coefficient of the extreme month (including extreme wet and months) precipitations within each year  
310 from 1988 to 2100, experiences significantly increasing trends ( $p < 0.01$ ), and increased from 0.76 /a over historical time from  
311 1998-2017, to 0.84 /a over future time from 2081 to 2100, by 10.53% with change rate of 0.01 /10a. The significantly increasing  
312 trends indicated the more uneven trend of precipitation in the temporal distribution, which might lead to increased risks of  
313 floods and droughts.

#### 314 **4.2.2 Daily precipitation changes**

315 To understand the changes in precipitation intensities and frequencies under future climate warming, daily precipitation  
316 variations were also analyzed and are shown in Fig. 8. Moderate vs extreme rain frequencies (Fig. 8a and b), the annual total  
317 rain vs the annual total rainy days (Fig. 8c), and the annual max precipitation vs the annual max continuous rainy days (Fig.  
318 8d) were analyzed.

319 Under climate warming, the annual frequency of moderate rains experienced decreasing trends; in contrast, the annual  
320 frequency of extreme rains experienced significantly increasing trends (Fig. 8a). Statistically, averaged over 103 years, annual  
321 precipitation frequencies are dominated by the moderate rain frequency a total of 163.70 days, or 44.8% (163.70/365), while  
322 the extreme rain occurs less often, a total of 20.70 days, or 6.70% (20.7/365). The remaining is rain-free days, a total of 180.75  
323 days, 49.5% (180.75/365). The annual moderate rain frequency decreased, from 170.56 days/a over the historical period from  
324 1998 to 2017, to 159.55 days/a over the future period from 2081 to 2100, by -6.46% with a change rate of -14.4 days/10a; on  
325 the contrary, the annual extreme rain frequency increased from 19.18 days/a over historical time from 1998 to 2017, to 23.42  
326 days/a over future time from 2081 to 2100, by 22.10% with a change rate of 0.49 days/10a (Fig. 8b).

327 Furthermore, the annual total rainy days, the sum of the moderate and extreme rain frequencies, demonstrated a significantly  
328 decreasing trend in the 21st century, whereas the annual total precipitation exhibited a significantly increasing trend (Fig. 7c).  
329 Rainy days decreased from 187.57 days/a over the historical period from 1998 to 2017, to 180.37 days/a over the future period  
330 from 2081 to 2100, by -3.84% with a change rate of -1.00 days/10a; while the annual total rain amount increased, from 1650  
331 mm/a over the historical period, from 1998 to 2017, to 1906 mm/a over the future period, from 2081 to 2100, by 15.55% with  
332 a change rate of 23.00 mm/10a. The increase in the annual total rain and decrease in the annual rainy days suggested more  
333 concentrated precipitation and dry days in the future. This tendency might lead to the increased risk of floods and droughts,  
334 which was also indicated by the increased annual max daily precipitation and max continuous dry days (Fig. 8d). Annual max  
335 daily precipitation increased from 148.76 mm•day<sup>-1</sup>/a averaged over the historical period from 1998 to 2017, to 212.01  
336 mm•day<sup>-1</sup>/a averaged over the future period from 2081 to 2100, by 42.51% with a change rate of 7.2 mm•day<sup>-1</sup>/10a; while the  
337 max continuous dry days increased from 25.35 days/a over the historical period from 1998 to 2017, to 28.15 days/a over the  
338 future period from 2081 to 2100, by 11.05% with a change rate of 0.5 days/10a.

339 Overall, the significantly inverse change trends in the moderate vs extreme rain frequencies, the annual total rain vs the annual  
340 total rainy days, and the annual max precipitation vs the annual max continuous rainy days, indicated an increasing temporal  
341 heterogeneity in precipitation distribution over the 21st century. Obviously, the increasing heterogeneity was exhibited by the  
342 increasing temporal variation coefficient of daily precipitations (Fig. 9). The temporal variation coefficient of daily  
343 precipitations increased from 1.50 /a over the historical period from 1998 to 2017, to 1.62 /a over the future period from 2081  
344 to 2100, by 7.48% with a change rate of 0.016 /10a.

### 345 **4.3 Spatial variation of future precipitation**

346 Climate warming could cause the rain belt shift (Putnam et al., 2017), which might lead to precipitation changes in the spatial  
347 pattern. To investigate the spatial variation, we analyzed the similarities and differences of precipitation changes in space (Fig.  
348 1); based on the differences, we use the indexes of the spatial and spatiotemporal variation coefficient to investigate the spatial  
349 heterogeneity changes (Fig. 11). Fig. 10 shows the precipitation changes in the spatial pattern during the period from 1998 to  
350 2100; Fig. 11 shows the spatial and spatiotemporal variation coefficient for each year over 1988 to 2100.

351 Precipitations showed a regular spatial pattern both in the wet and dry season, in Fig. 10a-c and e-g. More specifically,  
352 precipitation was distributed more in the east and west, however less in the north central plain and the south bottom depression.  
353 Rich rain in the east and west are dominated by the southeast and southwest summer monsoons. Less precipitation was due to  
354 the leeward sloop of the eastern (Xuefeng Mountain) and western mountains (Wuyi Mountain). Less precipitation in the south  
355 bottom depression was because that water vapor was blocked from this region by the NanLing Mountain in the south (Fig. 1a).  
356 The precipitation distribution in spatial pattern from 1998 to 2100 (Fig. 10 a-c and d-f) were consistent with the observations  
357 from 1951 to 2005 (Fig. 1b.), thus confirming the satisfactory performance of the STDDM. Moreover, wet and dry season  
358 precipitation showed inverse changes. The wet season precipitations exhibited ascending (Fig. 10a-c and g) change while the  
359 dry season precipitation exhibited descending (Fig. 10d-f and h) change from 1998 to 2100. The inverse changes were  
360 consistent with the interannual variability of increased precipitation in wet months and decreased precipitation in dry months  
361 (Section 4.2). The increase of precipitation in the wet seasons and decrease in precipitation in the dry seasons were also detected  
362 in the change rate of the cells over the entire watershed (Fig. 10g or h).  
363 However, precipitation change also showed a different spatial pattern. Precipitation change rate was heterogeneous in spatial  
364 distribution for dry or wet season respectively (Fig. 10g and h). In the wet season, the precipitation increased more in the north  
365 part of the watershed, except for the central plain (Fig. 10g); in the dry season, the precipitation decreased more in the central  
366 area (Fig. 10h). Statistically, in the wet season, precipitation increased with the change rate raising from  $\leq 3.6$  mm/10a in the  
367 southwest, to  $\geq 11.7$  mm/10a in the northeast; in the dry season, precipitation decreased with the change rate falling from  $\geq -$   
368  $2.0$  mm/10a in the surrounding region, to  $\leq -2.7$  mm/10a in the central region. Furthermore, precipitation changes show  
369 different spatial characteristics in wet and dry seasons. From 1998 to 2100, in the wet season (Fig. 10a-c), the wet area (the  
370 reddish area, mainly in the north except for the center plain) becomes wetter; in the dry season (Fig. 10 d-f), the dry area (the  
371 bluish area, mainly in the north center plain and in the south depression) become drier.  
372 The uneven change rates may lead to increase of the spatial heterogeneity of precipitation under global warming, and the  
373 tendency of the wet area to become wetter and the dry area to become drier also indicated the increasing spatiotemporal  
374 heterogeneity of precipitations. Indeed, the spatial heterogeneity did increase, with the spatial variation coefficients raising  
375 from  $0.097/a$  over the historical period (1998-2017), to  $0.110/a$  over the future period (2081-2100), by 12.64% with a change



376 rate of 0.002 /10a (Fig. 11a). The spatiotemporal heterogeneity did increase with the spatiotemporal variation coefficient  
377 raising from 0.89 /a over the historical period (1998-2017), to 0.94 /a over the future period (2081-2100), by 4.96% with a  
378 change rate of 0.008 /10a. Overall, the uneven change rates for the whole basin and inverse changes for the dry and wet area  
379 indicated an increasing spatial heterogeneity in precipitation distribution over the 21st century.

#### 380 **4.4 The impact assessment of temperature increment on precipitation changes**

381 Previous studies have detected precipitation changes and have attributed these changes to climate warming (Westra et al., 2013;  
382 Zhang et al., 2013). In this study, the spatiotemporal changes of precipitation in the Poyang Lake Watershed in the 21st century  
383 were hypothesized to be related to temperature increments. So we analyze the correlations qualitatively and quantitatively.

384 The following are trying to demonstrate the driving force related to climate warming on precipitation changes in the temporal  
385 pattern. In the wet season from April to July, the summer monsoon might become weaker in Southeast Asia as the temperature  
386 increasing (Wang, 2001; Wang, 2002; Guo et al., 2003). Consequently, the summer monsoon is delayed for a longer time in  
387 the middle and lower Yangtze River basin instead of moving further north. The delay leads to much more rain during the wet  
388 season. As being located in the middle of the Yangtze River basin, the Poyang Lake Watershed becomes wetter in the wet  
389 season (Fig. 5-5, Fig. 10a-c). In fact, the increase in precipitation in the Poyang Lake Watershed was detected in previous  
390 studies (Yu and Zhou, 2007; Ding et al., 2008). In the dry period from September to the subsequent February (especially in  
391 the winter season, from December to February), during which summer monsoon is inactive, there is less water vapor in the  
392 atmosphere to condense into rain. Additionally, stronger winds in the winter (Wu et al., 2013) blow the evaporation away, thus  
393 enhancing the difficulty of generating rain from water vapor compared to the other seasons. When temperature increases, the  
394 ability of the atmosphere to hold water vapors is strengthened, which makes it more difficult to precipitate. Therefore,  
395 precipitation decreases in the dry season, consistent with Li et al.'s (2016) result. As temperature increment increases the ability  
396 of the atmosphere to contain water vapor, rain is more difficult, and if it rains it will rain largely (Min et al., 2011; Zhang et  
397 al., 2013). Thus, the frequency of heavy rain and rain-free events increases, indicating increased frequency and strengthened  
398 intensity of the extreme precipitation. Overall, the climate warming might make precipitation more temporally uneven.

399 Climate warming could also explain the spatial distribution of precipitation changes in the dry and wet seasons. In the wet  
400 season, the summer monsoon delays in the middle and lower Yangtze River Basin. The delaying area covers only the north  
401 part of the Poyang Lake Watershed. As it receives abundant water vapor from the delayed summer monsoon, the north part of  
402 Poyang Lake Watershed experiences a greater increase in precipitation with a larger change rate (Fig. 10g). The eastern Poyang  
403 Lake Watershed is the nearest to the western Pacific Ocean; thus the eastern region receives more continuous water vapor. So  
404 the precipitation change rate decreases from the southeast to the northwest in the wet season. However, in the dry season  
405 especially in winter, during which there is a low-frequency or absent summer monsoon, the water vapor mainly comes from  
406 evapotranspiration. In the watershed, the periphery is covered by the lake of Poyang in the northern plain and high-density  
407 vegetation in the northwest, southeast and southwest mountains; so there is more evapotranspiration in the periphery. The  
408 center is mainly covered by farmland and grassland; so there is less evapotranspiration in the center (Wu et al., 2013). Thus,  
409 the moisture decreases from the surrounding to the center. Therefore, as temperature increases, it is more difficult for rain to  
410 occur in the area of lower moisture, the center of the Poyang Lake Watershed. Therefore the precipitation decreased with a  
411 change rate falling from the surrounding to the center in the dry season (Fig. 10h).

412 To quantitatively analyze the relationship between precipitation changes and temperature increment, we created a scatter plot  
413 between precipitation indexes changes and temperature increment, as shown in Fig. 12. A trend analysis was conducted using  
414 linear regression of each annual precipitation index over the 103 years from 1998 to 2100. The associated slopes represent the  
415 change rate of each precipitation index relative to temperature increment. The significance of the trend is indicated by p value.  
416 As shown in Fig. 12, there is a significant correlation between the precipitation change and the temperature increment, with  $p$   
417  $\leq 0.001$  and  $R \geq 0.78$  for 6 precipitation indexes: the annual precipitation in the wet season (Fig. 12a), the annual max daily  
418 precipitation (Fig. 12d), the temporal variation coefficient of the monthly precipitation (Fig. 12c), the temporal variation  
419 coefficient of the daily precipitation (Fig. 12f), the spatial variation coefficient (Fig. 12g) and the spatiotemporal variation  
420 coefficient (Fig. 12h). However, changes of the other two precipitation indexes, the annual precipitation in the dry season (Fig.  
421 12b) and the annual max continuous dry days (Fig. 12e), appeared to be correlated with slight signs of  $p \leq 0.05$  and  $R \leq 0.58$ .  
422 The overestimation of moderate- or free-rain frequency from the GCM simulations (Teutschbein et al. 2012) might explain  
423 the slightly low correlation between the annual precipitation values in the dry season and temperature increment, while the

424 overestimation of the precipitation frequencies (Prudhomme et al. 2003) could explain the slightly low correlation between the  
425 annual max continuous dry days and temperature increment. For all the correlations (Fig. 12a-h), the precipitation changed  
426 with fluctuation, which might be caused by random variations from GCMs.

427 Overall, despite the low correlations and stochastic fluctuation, the correlations could indicate that the climate warming can  
428 partly explain the precipitation changes. Statistically, precipitation changes relative to temperature increment are 16.657  
429  $\text{mm}\cdot\text{month}^{-1}/\text{K}$ ,  $-4.31 \text{ mm}\cdot\text{month}^{-1}/\text{K}$ ,  $17.45 \text{ mm}\cdot\text{day}^{-1}/\text{K}$ ,  $0.71 \text{ days}/\text{K}$ ,  $0.028/\text{K}$ ,  $0.033/\text{K}$ ,  $0.0074/\text{K}$  and  $0.02/\text{K}$  for the annual  
430 precipitation in the wet season, the annual precipitation in the dry season, the annual max daily precipitation, the annual max  
431 continuous dry days, the temporal variation coefficient of the monthly precipitation, the temporal variation coefficient of the  
432 daily precipitation, and the spatial variation coefficient and the spatiotemporal variation coefficient, respectively.

433 In summary, the explanation of precipitation changes in temporal and spatial distribution qualitatively and quantitatively,  
434 suggests the downscaling method is reasonable and the STDDM could be applied in the basin-scale region based on a GCM  
435 successfully.

## 436 **5 Conclusion**

437 A spatiotemporally distributed downscaling method (STDDM) was proposed in this study. The downscaling method  
438 considered the heterogeneity in spatial and temporal distributions, and produced local climate variables as spatially continuous  
439 data instead of independent and discrete points. The STDDM showed a better performance than the No-STDDM. Using the  
440 STDDM, we constructed the spatially continuous future precipitation distribution and dynamics in the wet and dry season from  
441 1998 to 2100, based on MRI-CGCM3. Several findings were obtained:

442 First, the spatial and temporal heterogeneity of precipitation increased under future climate warming. In the temporal pattern,  
443 the wet season become wetter, while the dry season become drier. The frequency of extreme precipitation increased, while  
444 that of the moderate precipitation decreased. Total precipitation increased, while rain days decreased. The max dry day number  
445 and the max daily precipitation both increased. These precipitation changes demonstrated an increasing heterogeneity of  
446 precipitation in temporal distribution, and the change rate of temporal heterogeneity is  $0.01/10\text{a}$  ( $0.016/10\text{a}$ ) for the temporal  
447 variation coefficient of the monthly (daily) precipitation. In the spatial pattern, the change rate of precipitation was uneven

448 over the whole watershed. Additionally, the wet areas become wetter in the wet season and the dry areas become drier in the  
449 dry season. The uneven change rates for the whole basin and inverse change for dry and wet area demonstrated an increasing  
450 heterogeneity in the spatial distribution, and the change rate of spatial heterogeneity was 0.002/10a.

451 Second, precipitation changes can be significantly explained by climate warming, with  $p < 0.05$  and  $R \geq 0.56$ . The explanation  
452 of precipitation changes in temporal and spatial distribution qualitatively and quantitatively, suggests the downscaling method  
453 is reasonable and the STDDM could be applied in the basin-scale region based on a GCM successfully.

454 The results can be applied to a hydrological and hydrodynamic model, to study the future changes in water volumes, lake  
455 levels and areas response to climate warming. The relationship between precipitation variations and temperature increment  
456 could be helpful to the driving forces analysis of precipitation changes. The dry to be drier and wet to be wetter condition may  
457 lead to increased risk of floods and droughts. In particular, in the region where floods and droughts do not usually occur,  
458 additional adaptation measures could be taken to prevent loss from the future frequent hydrological disasters.

#### 459 **Data availability**

460 All data can be accessed as described in Sect. 2.2. The data sets and model codes are provided in the supplements.

#### 461 **Acknowledgements**

462 This work was funded by the National Key Research and Development Program (2017YFB0504103), the National Natural  
463 Science Funding of China (NSFC) (41331174), the Open Foundation of Jiangxi Engineering Research Center of Water  
464 Engineering Safety and Resources Efficient Utilization (OF201601), the ESA-MOST Cooperation DRAGON 4 Project  
465 (EOWAQYWET), the Fundamental Research Funds for the Central Universities (2042018kf0220) and the LIESMARS  
466 Special Research Funding.

467 **Reference**

- 468 Alexander, L. V., Zhang, X., Peterson, T. ., Caesar, J., Gleason, B., Klein Tank, A. M. G., Haylock, M. R., Collins, W. D. and  
469 Trewin, B.: Global observed changes in daily climate extremes of temperature and precipitation, *J. Geophys. Res.*, 111, D05109,  
470 doi:10.1029/2005JD006290, 2006.
- 471 Baigorria, G. A. and Jones, J. W.: GiST: A Stochastic Model for Generating Spatially and Temporally Correlated Daily  
472 Rainfall Data, *J. Clim.*, 23(22), 5990–6008, doi: 10.1175/2010jcli3537.1, 2010.
- 473 Ben Alaya, M. A., Ouarda, T. B. M. J. and Chebana, F.: Non-Gaussian spatiotemporal simulation of multisite daily  
474 precipitation: downscaling framework, *Clim. Dyn.*, 50(1–2), doi:10.1007/s00382-017-3578-0, 2018.
- 475 Beven, K. J.: A Discussion of distributed hydrological modelling, *Distrib. Hydrol. Model.*, 255–278, doi:10.1007/978-94-009-  
476 0257-2\_13, 1996.
- 477 Boé, J., Terray, L., Habets, F. and Martin, E.: Statistical and dynamical downscaling of the Seine basin climate for hydro-  
478 meteorological studies, *Int. J. Climatol.*, 27(12), 1643–1655, doi:10.1002/joc.1602, 2007.
- 479 Charles, S. P., Bates, B. C. and Hughes, J. P.: A spatiotemporal model for downscaling precipitation occurrence and amounts,  
480 *J. Geophys. Res. Atmos.*, 104(D24), 31657–31669, doi:10.1029/1999JD900119, 1999.
- 481 Chen, H. and Sun, J.: How the “best” models project the future precipitation change in China, *Adv. Atmos. Sci.*, 26(4), 773–  
482 782, doi:10.1007/s00376-009-8211-7, 2009.
- 483 Chen, J., Chen, H. and Guo, S.: Multi-site precipitation downscaling using a stochastic weather generator, *Clim. Dyn.*, 50(5–  
484 6), 1975–1992, doi:10.1007/s00382-017-3731-9, 2018.
- 485 Chu, J. T., Xia, J., Xu, C. Y. and Singh, V. P.: Statistical downscaling of daily mean temperature, pan evaporation and  
486 precipitation for climate change scenarios in Haihe River, China, *Theor. Appl. Climatol.*, 99(1–2), 149–161,  
487 doi:10.1007/s00704-009-0129-6, 2010.
- 488 Cowpertwait, P. S. P.: A space-time Neyman-Scott model of rainfall: Empirical analysis of extremes, *Water Resour. Res.*,  
489 38(8), 6-1-6–14, doi:10.1029/2001WR000709, 2002.
- 490 Dai, A.: Increasing drought under global warming in observations and models, *Nat. Clim. Chang.*, 3(1), 52–58,  
491 doi:10.1038/nclimate1633, 2013.

492 DHI (Danish Hydraulic Institute): MIKE SHE, User Manual, Volume 1: User Guide. Hørsholm: Danish Hydraulic Institute,  
493 2014.

494 Dyderski, M. K., Paż, S., Frelich, L. E. and Jagodziński, A. M.: How much does climate change threaten European forest tree  
495 species distributions?, *Glob. Chang. Biol.*, doi:10.1111/gcb.13925, 2017.

496 Engman, E. T.: Remote sensing in hydrology, *Geophys. Monogr. Ser.*, 108, 165–177, doi:10.1029/GM108p0165, 1998.

497 Enke, W., Schneider, F. and Deutschländer, T.: A novel scheme to derive optimized circulation pattern classifications for  
498 downscaling and forecast purposes, *Theor. Appl. Climatol.*, 82(1–2), 51–63, doi:10.1007/s00704-004-0116-x, 2005.

499 Feng, L., Hu, C., Chen, X., Cai, X., Tian, L. and Gan, W.: Assessment of inundation changes of Poyang Lake using MODIS  
500 observations between 2000 and 2010, *Remote Sens. Environ.*, 121, 80–92, doi:10.1016/j.rse.2012.01.014, 2012a.

501 Feng, L., Hu, C., Chen, X., Tian, L. and Chen, L.: Human induced turbidity changes in Poyang Lake between 2000 and 2010:  
502 Observations from MODIS, *J. Geophys. Res. Ocean.*, 117(7), doi:10.1029/2011JC007864, 2012b.

503 Ferraris, L., Gabellani, S., Rebori, N. and Provenzale, A.: A comparison of stochastic models for spatial rainfall downscaling,  
504 *Water Resour. Res.*, 39(12), doi:10.1029/2003WR002504, 2003.

505 Fowler, H. J., Blenkinsop, S. and Tebaldi, C.: Linking climate change modelling to impacts studies: Recent advances in  
506 downscaling techniques for hydrological modelling, *Int. J. Climatol.*, 27(12), 1547–1578, doi:10.1002/joc.1556, 2007.

507 Giorgi, F.: Simulation of Regional Climate Using a Limited Area Model Nested in a General Circulation Model, *J. Clim.*, 3(9),  
508 941–963, doi:10.1175/1520-0442(1990)003<0941:SORCUA>2.0.CO;2, 1990.

509 Grotch, S. L. and MacCracken, M. C.: The Use of General Circulation Models to Predict Regional Climatic Change, *J. Clim.*,  
510 4(3), 286–303, doi:10.1175/1520-0442(1991)004<0286:TUOGCM>2.0.CO;2, 1991.

511 Guillot, G. and Lebel, T.: Disaggregation of Sahelian mesoscale convective system rain fields: Further developments and  
512 validation, *J. Geophys. Res. Atmos.*, 104(D24), 31533–31551, doi:10.1029/1999JD900986, 1999.

513 Guo, J.L., Guo, S., Guo, J., Chen, H.: Prediction of Precipitation Change in Poyang Lake Basin. *Journal of Yangtze River*  
514 *Scientific Research Institute*, 8, 007, 2010.

515 Han, X., Chen, X. and Feng, L.: Four decades of winter wetland changes in Poyang Lake based on Landsat observations  
516 between 1973 and 2013, *Remote Sens. Environ.*, 156, 426–437, doi:10.1016/j.rse.2014.10.003, 2014.

517 Hong X, Guo S, Guo J, et al. Projected changes of extreme precipitation characteristics in the Poyang Lake Basin based on  
518 statistical downscaling model. *Journal of Water Resources Research*, 3(6), 511-521, doi:10.12677/JWRR.2014.36063, 2014.

519 Hutchinson, M. F.: Interpolation of Rainfall Data with Thin Plate Smoothing Splines - Part I : Two dimensional Smoothing of  
520 Data with Short Range Correlation, *J. Geogr. Inf. Decis. Anal.*, 2(2), 152–167, doi:10.1.1.13.6255, 1998.

521 Hutchinson, M. F.: Interpolation of Rainfall Data with Thin Plate Smoothing Splines - Part II: Analysis of Topographic  
522 Dependence, *J. Geogr. Inf. Decis. Anal.*, 2(2), 152–167, 1998.

523 Leander, R. and Buishand, T. A.: Resampling of regional climate model output for the simulation of extreme river flows, *J.*  
524 *Hydrol.*, 332(3–4), 487–496, doi:10.1016/j.jhydrol.2006.08.006, 2007.

525 Lenderink, G., Buishand, A. and Van Deursen, W.: Estimates of future discharges of the river Rhine using two scenario  
526 methodologies: Direct versus delta approach, *Hydrol. Earth Syst. Sci.*, 11(3), 1145–1159, doi:10.5194/hess-11-1145-2007,  
527 2007.

528 Li, H., Sheffield, J. and Wood, E.: Bias correction of monthly precipitation and temperature fields from Intergovernmental  
529 Panel on Climate Change AR4 models using equidistant quantile, *J. Geophys. Res.*, 115(10), D10101,  
530 doi:10.1029/2009JD012882, 2010.

531 Li, Y. L., Tao, H., Yao, J. and Zhang, Q.: Application of a distributed catchment model to investigate hydrological impacts of  
532 climate change within Poyang Lake catchment (China), *Hydrol. Res.*, 47(S1), 120–135, doi:10.2166/nh.2016.234, 2016.

533 Liang X, Lettenmaier D P, Wood E F, et al. A simple hydrologically based model of land surface water and energy fluxes for  
534 general circulation models [J]. *Journal of Geophysical Research: Atmospheres*, 99(D7): 14415-14428, 1994.

535 Liu, C. M., Liu, W. Bin, Fu, G. Bin and Ouyang, R. L.: A discussion of some aspects of statistical downscaling in climate  
536 impacts assessment, *Shuikexue Jinzhan/Advances Water Sci.*, 23(3), 427–437, doi:CNKI: 32.1309.P.20120501.1616.002,  
537 2012.

538 Lovejoy, S. and Schertzer, D.: Multifractals, cloud radiances and rain, *J. Hydrol.*, 322(1–4), 59–88,  
539 doi:10.1016/j.jhydrol.2005.02.042, 2006.

540 Manzanas, R., Lucero, A., Weisheimer, A. and Gutiérrez, J. M.: Can bias correction and statistical downscaling methods  
541 improve the skill of seasonal precipitation forecasts?, *Clim. Dyn.*, 50(3–4), 1161–1176, doi:10.1007/s00382-017-3668-z, 2018.

542 Maurer, E. P. and Hidalgo, H. G.: Utility of daily vs. monthly large-scale climate data: An intercomparison of two statistical  
543 downscaling methods, *Hydrol. Earth Syst. Sci.*, 12(2), 551–563, doi:10.5194/hess-12-551-2008, 2008.

544 Min, Q., Min, D.: Drought Change Characteristics and Drought Protection Countermeasures for Poyanghu Lake Basin, *Journal*  
545 *of China Hydrology*, 1, 84-88, 2010.

546 Min, S. K., Zhang, X., Zwiers, F. W. and Hegerl, G. C.: Human contribution to more-intense precipitation extremes, *Nature*,  
547 470(7334), 378–381, doi:10.1038/nature09763, 2011.

548 Mullan, D., Chen, J. and Zhang, X. J.: Validation of non-stationary precipitation series for site-specific impact assessment:  
549 comparison of two statistical downscaling techniques, *Clim. Dyn.*, 46(3–4), 967–986, doi:10.1007/s00382-015-2626-x, 2016.

550 Pall, P., Aina, T., Stone, D. A., Stott, P. A., Nozawa, T., Hilberts, A. G. J., Lohmann, D. and Allen, M. R.: Anthropogenic  
551 greenhouse gas contribution to flood risk in England and Wales in autumn 2000, *Nature*, 470(7334), 382–385,  
552 doi:10.1038/nature09762, 2011.

553 Prudhomme, C., Reynard, N. and Crooks, S.: Downscaling of global climate models for flood frequency analysis: Where are  
554 we now, *Hydrol. Process.*, 16, 1137–1150, 2002.

555 Putnam, A. E. and Broecker, W. S.: Human-induced changes in the distribution of rainfall, *Sci. Adv.*, 3(5),  
556 doi:10.1126/sciadv.1600871, 2017.

557 Riahi, K., Rao, S., Krey, V., Cho, C., Chirkov, V., Fischer, G., Kindermann, G., Nakicenovic, N. and Rafaj, P.: RCP 8.5-A  
558 scenario of comparatively high greenhouse gas emissions, *Clim. Change*, 109(1), 33–57, doi:10.1007/s10584-011-0149-y,  
559 2011.

560 Segu, P. Q.: Comparison of three downscaling methods in simulating the impact of climate change on the hydrology of  
561 Mediterranean basins, *J. Hydrol.*, 383, 111–124, 2010.

562 Sibson, R: A brief description of natural neighbour interpolation. *Interpreting multivariate data*, 1981.

563 Sperber, K. R., Annamalai, H., Kang, I. S., Kitoh, A., Moise, A., Turner, A., Wang, B. and Zhou, T.: The Asian summer  
564 monsoon: An intercomparison of CMIP5 vs. CMIP3 simulations of the late 20th century, *Clim. Dyn.*, 41(9–10), 2711–2744,  
565 doi:10.1007/s00382-012-1607-6, 2013.



566 Tan, Ruizhi: A Study on the Regional Energetics during Break, Transitional and Active Periods of the Southwest Monsoon in  
567 South East Asia, *SCIENTIA ATMOSPHERICA SINICA*, 1994.

568 Taylor, K. E., Stouffer, R. J. and Meehl, G. A.: An overview of CMIP5 and the experiment desing. *American Meteorological*  
569 *Society, Bulletin Am. Meteorol. Soc.*, 93, 485–498, doi:10.1175/BAMS-D-11-00094.1, 2012.

570 Teutschbein, C. and Seibert, J.: Bias correction of regional climate model simulations for hydrological climate-change impact  
571 studies: Review and evaluation of different methods, *J. Hydrol.*, 456–457, 12–29, doi:10.1016/j.jhydrol.2012.05.052, 2012.

572 Teutschbein, C. and Seibert, J.: Is bias correction of regional climate model (RCM) simulations possible for non-stationary  
573 conditions, *Hydrol. Earth Syst. Sci.*, 17(12), 5061–5077, doi:10.5194/hess-17-5061-2013, 2013.

574 Toggweiler, J. and Key, R.: Ocean circulation: Thermohaline circulation, *Encycl. Atmos. Sci.*, 4, 1549–1555., doi:10.1002/joc,  
575 2001.

576 Trenberth K E.: Changes in precipitation with climate change, *Clim. Res.*, 47(1–2), 123–138, 2011.

577 Trzaska, S. and Schnarr, E.: A Review of Downscaling Methods for Climate Change Projections, *Review*, (September), 1–42,  
578 doi:10.4236/ojog.2016.613098, 2014.

579 Wang H, Zhao G, Peng J, et al.: Precipitation characteristics over five major river systems of Poyang drainage areas in recent  
580 50 years. *Resources and Environment in the Yangtze Basin*, 7, 615-619, 2009.

581 Wang, J., Hong, Y., Li, L., Gourley, J. J., Khan, S. I., Yilmaz, K. K., Adler, R. F., Policelli, F. S., Habib, S., Irwn, D., Limaye,  
582 A. S., Korme, T. and Okello, L.: The coupled routing and excess storage (CREST) distributed hydrological model, *Hydrol.*  
583 *Sci. J.*, 56(1), 84–98, doi:10.1080/02626667.2010.543087, 2011.

584 Weisheimer, R. M. A. L. A. and Gutiérrez, J. M.: Can bias correction and statistical downscaling methods improve the skill of  
585 seasonal precipitation forecasts ?, *Clim. Dyn.*, 50(3), 1161–1176, doi:10.1007/s00382-017-3668-z, 2018.

586 Wheeler, H. S., Chandler, R. E., Onof, C. J., Isham, V. S., Bellone, E., Yang, C., Lekkas, D., Lourmas, G. and Segond, M. L.:  
587 Spatial-temporal rainfall modelling for flood risk estimation, *Stoch. Environ. Res. Risk Assess.*, 19(6), 403–416,  
588 doi:10.1007/s00477-005-0011-8, 2005.

589 Wilby, R. and Dawson, C. W.: SDSM 4.2-A decision support tool for the assessment of regional climate change impacts, 94,  
590 2007.

591 Wilks, D. S.: Use of stochastic weather generators for precipitation downscaling, *Wiley Interdiscip. Rev. Clim. Chang.*, 1(6),  
592 898–907, doi:10.1002/wcc.85, 2010.

593 WU, G., LIU, Y., ZHAO, X., & YE, C.: Spatio-temporal variations of evapotranspiration in Poyang Lake Basin using MOD16  
594 products, *Geographical Research*, 32(4), 617-627, 2013.

595 Wu, J., Zha, J. and Zhao, D.: Evaluating the effects of land use and cover change on the decrease of surface wind speed over  
596 China in recent 30 years using a statistical downscaling method, *Clim. Dyn.*, 48(1–2), 131–149, doi:10.1007/s00382-016-  
597 3065-z, 2017.

598 Wu, Q., Nie, Q., Zhou, R.: Analysis of wind energy resources reserves and characteristics in mountain area of Jiangxi province,  
599 *Journal of Natural Resources*, 28(9), 1605-1614, doi: 10.11849/zrzyxb.2013.09.015, 2013.

600 Xu, C. Y.: From GCMs to river flow: A review of downscaling methods and hydrologic modelling approaches, *Prog. Phys.*  
601 *Geogr.*, 23(2), 229–249, doi:10.1191/030913399667424608, 1999.

602 Ye, X., Zhang, Q., Bai, L. and Hu, Q.: A modeling study of catchment discharge to Poyang Lake under future climate in China,  
603 *Quat. Int.*, 244(2), 221–229, doi:10.1016/j.quaint.2010.07.004, 2011.

604 Yuan, W.: Diurnal cycles of precipitation over subtropical China in IPCC AR5 AMIP simulations, *Adv. Atmos. Sci.*, 30(6),  
605 1679–1694, doi:10.1007/s00376-013-2250-9, 2013.

606 Yukimoto, S., Adachi, Y., Hosaka, M., et al.: A New Global Climate Model of the Meteorological Research Institute: MRI-  
607 CGCM3-Model Description and Basic Performance, *J. Meteorol. Soc. Japan*, 90A, 23–64, doi:10.2151/jmsj.2012-A02, 2012.

608 Zhan, M., Yin, J. and Zhang, Y.: Analysis on characteristic of precipitation in Poyang Lake Basin from 1959 to 2008, *Procedia*  
609 *Environ. Sci.*, 10, 1526–1533, doi:10.1016/j.proenv.2011.09.243, 2011.

610 Zhang, L., Lu, J., Chen, X., Liang, D., Fu, X., Sauvage, S. and Perez, J. M. S.: Stream flow simulation and verification in  
611 ungauged zones by coupling hydrological and hydrodynamic models: A case study of the Poyang Lake ungauged zone, *Hydrol.*  
612 *Earth Syst. Sci.*, 21(11), 5847–5861, doi:10.5194/hess-21-5847-2017, 2017.

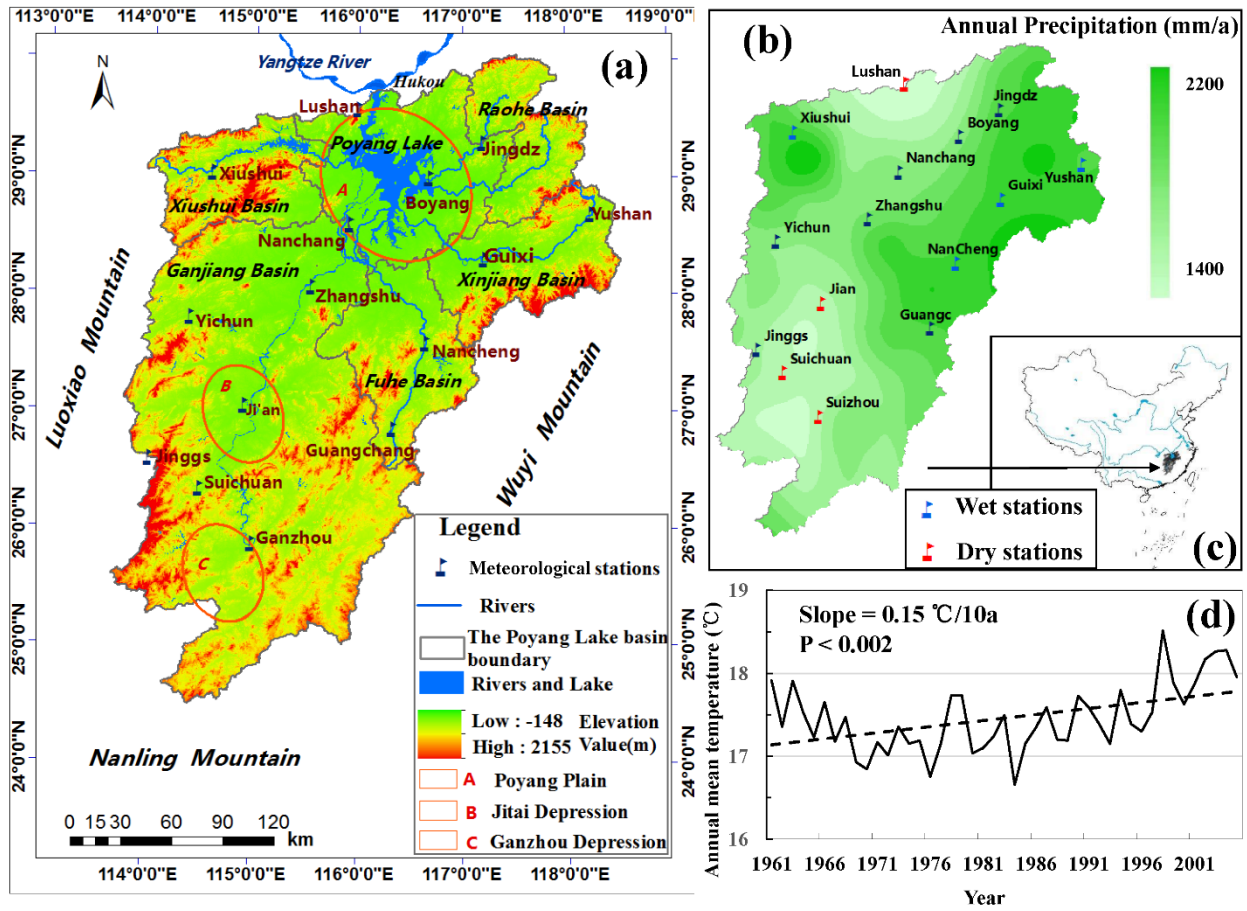
613 Zhang, Q., Ye, X. chun, Werner, A. D., Li, Y. liang, Yao, J., Li, X. hu and Xu, C. yu: An investigation of enhanced recessions  
614 in Poyang Lake: Comparison of Yangtze River and local catchment impacts, *J. Hydrol.*, 517, 425–434,  
615 doi:10.1016/j.jhydrol.2014.05.051, 2014.

616 Zhang, X. C.: Spatial downscaling of global climate model output for site-specific assessment of crop production and soil  
617 erosion, *Agric. For. Meteorol.*, 135(1–4), 215–229, doi:10.1016/j.agrformet.2005.11.016, 2005.

618 Zhang, X., Wan, H., Zwiers, F. W., Hegerl, G. C. and Min, S. K.: Attributing intensification of precipitation extremes to human  
619 influence, *Geophys. Res. Lett.*, 40(19), 5252–5257, doi:10.1002/grl.51010, 2013.

620 Zhao, Y., Zhu, J. and Xu, Y.: Establishment and assessment of the grid precipitation datasets in China for recent 50 years, *J.*  
621 *Meteorol. Sci.*, 34(4), 4–10, 2014.

622 Zorita, E. and Von Storch, H.: The analog method as a simple statistical downscaling technique: Comparison with more  
623 complicated methods, *J. Clim.*, 12, 2474–2489, doi:10.1175/1520-0442(1999)012<2474:TAMAAS>2.0.CO;2, 1999.



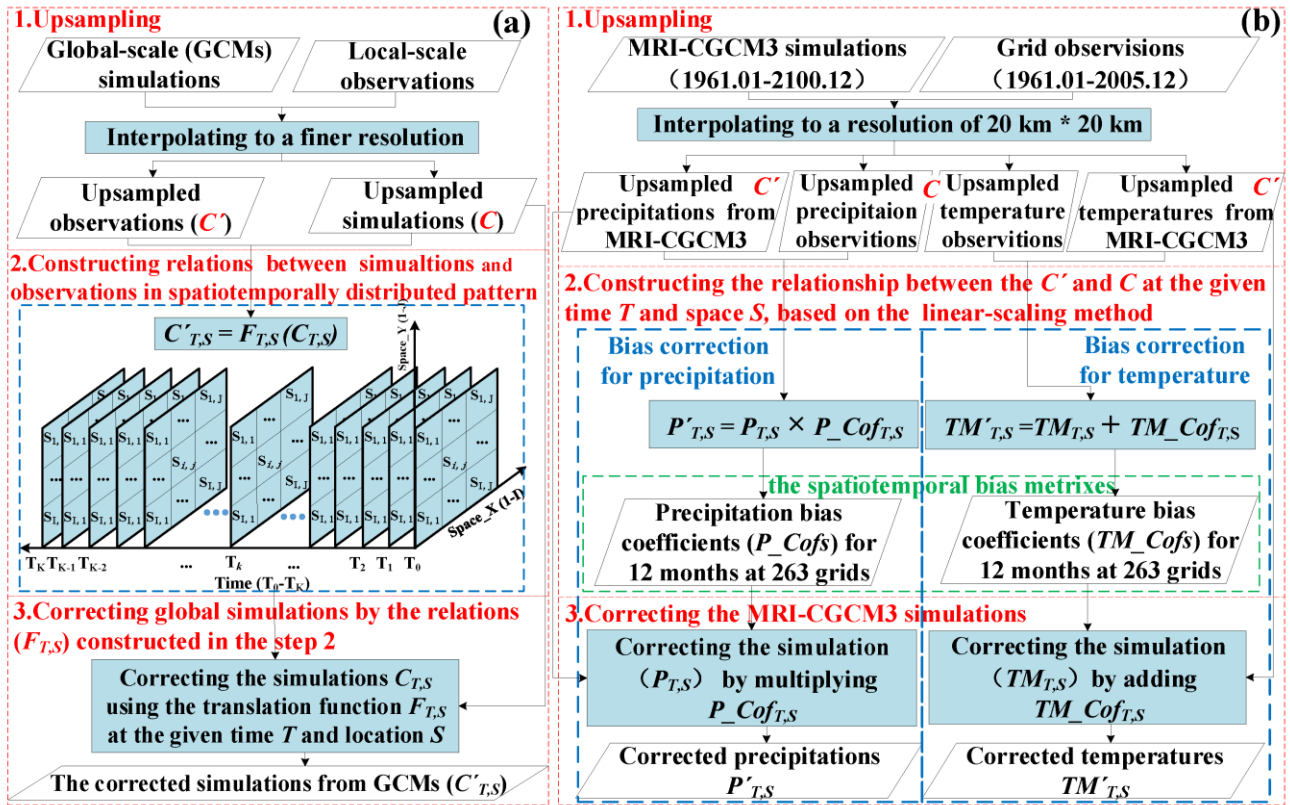
625

626 Fig. 1. The topography and landforms (a), precipitation distribution and dry-wet stations (b), temperature change (d) and

627 location of the Poyang Lake Basin (c). We sorted the annually accumulated precipitation of the 15 stations, averaged over time

628 from 1961 to 2005. The 4 stations with the max or min mean annual precipitations are set as dry or wet stations, respectively.

629



630

631

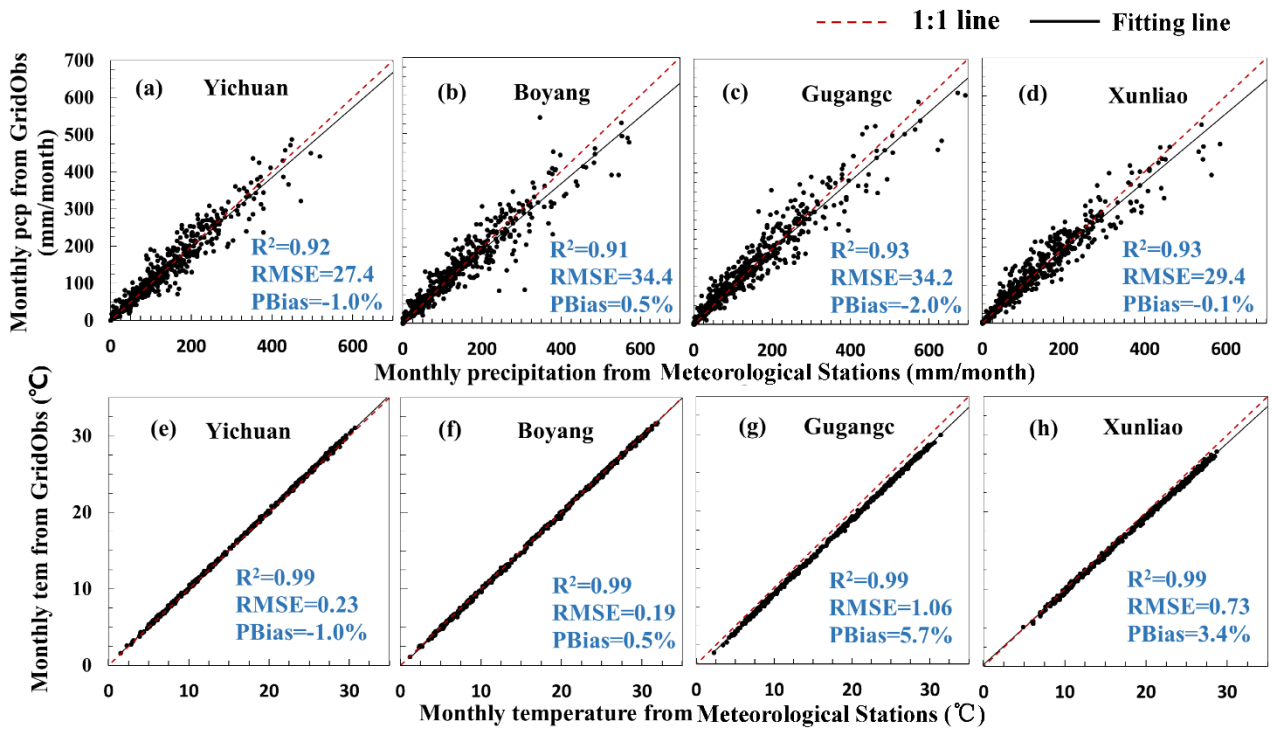
632

633

634

635

Fig. 2 Conceptual flow chart of the climate projection including upsampling, relation construction and correction: The common framework of the STDDM (a) and test case base on the linear-scaling algorithm (b). The STDDM was used to project MRI-CGCM3 simulations from 1998 to 2100.



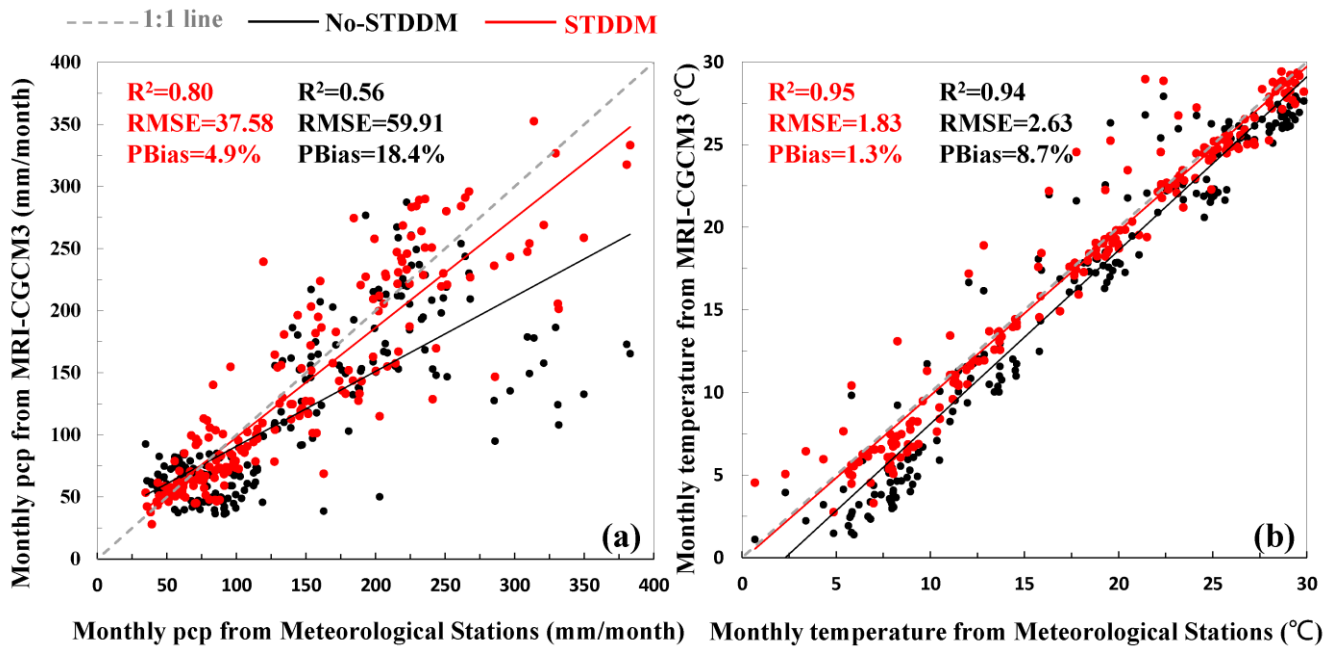
636

637

638

639

Fig. 3. Validation of gridded meteorological data (GridObs) by using gauging stations observation: Precipitation (pcp; a,b,c and d) and temperature (tem; e,d,f and g) at meteorological station of Jian (a and e), Ganzhou (b and d), Zhangshu (c and f) and Lushan (d and g).



640

641

642

643

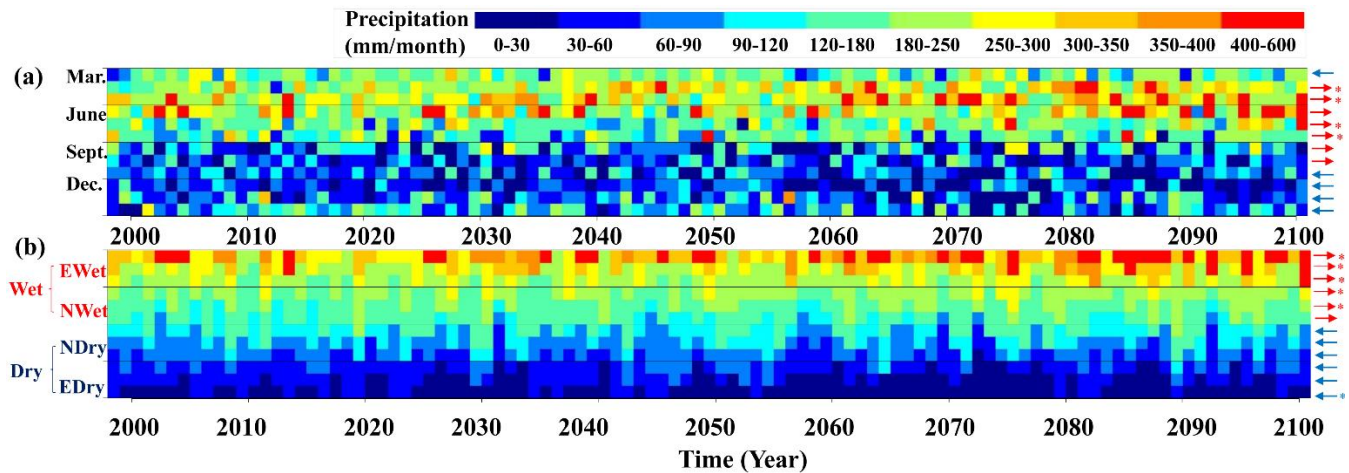
644

645

646

647

Fig. 4. Validation of the precipitation (pcp) (a) and temperature (b) projections by the STDDM (in black) and No-STDDM (in red). Dots represent the monthly precipitations (or temperatures), averaged over 20 years from 1986 to 2005. The dots contain monthly precipitations of the 15 stations. The solid lines represent linear regression which is the best fit through all match-ups of the projections and observations.

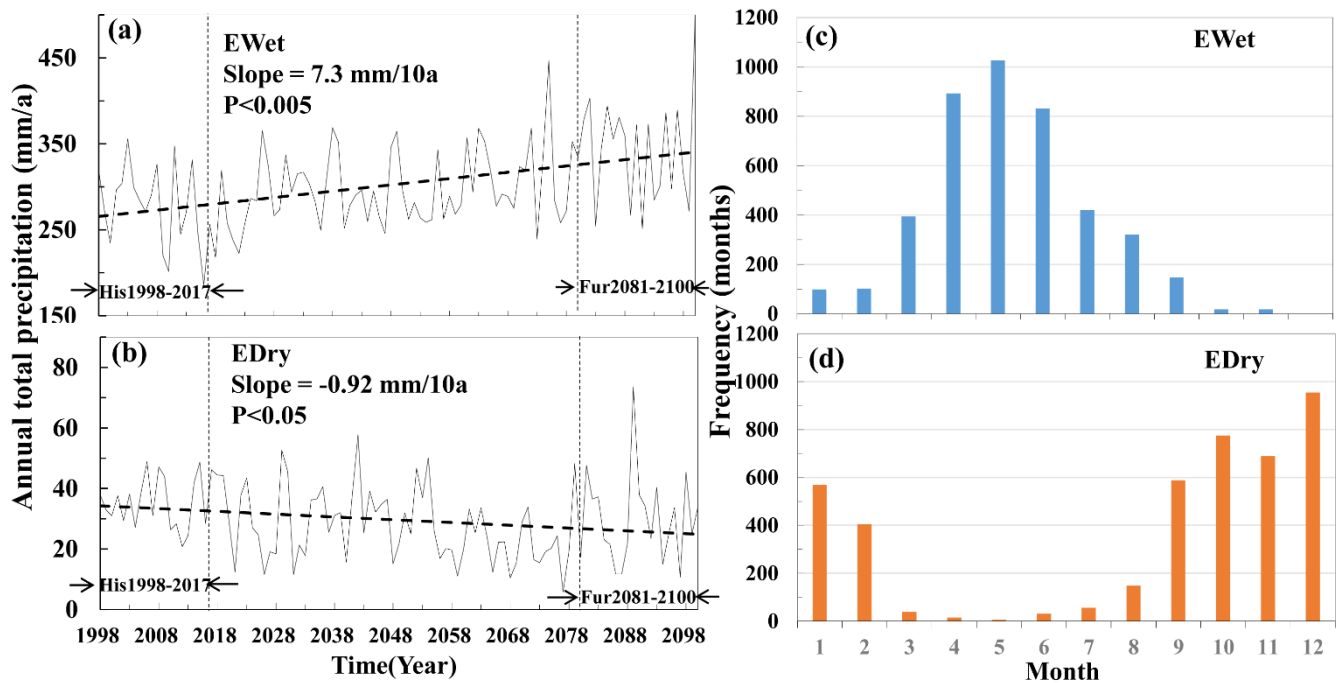


648

649 Fig. 5. Total variability of monthly precipitation from 1998 to 2100. Each column represents the data for one year and each  
 650 cell represents an accumulative precipitation of one month. The red (blue) arrows indicate that the monthly precipitation  
 651 experienced an increasing (decreasing) trend over the 103 years, respectively. The asterisk demonstrates the significant trends  
 652 with  $p < 0.05$ . (a) Monthly precipitation in month order, referred to Spring (March to May), summer (June to August), autumn  
 653 (September to November), and winter (December to next February) from top to bottom, respectively. (b) Monthly precipitation,  
 654 sorted in the descending order for each year, where months are classified as extreme wet (EWet), normal wet (NWet), normal  
 655 dry (NDry) and extreme dry (EDry) months from up to down. Therein, wet months (Wet) include extreme and normal wet ones  
 656 while dry months (Dry) include extreme and normal dry ones.

657

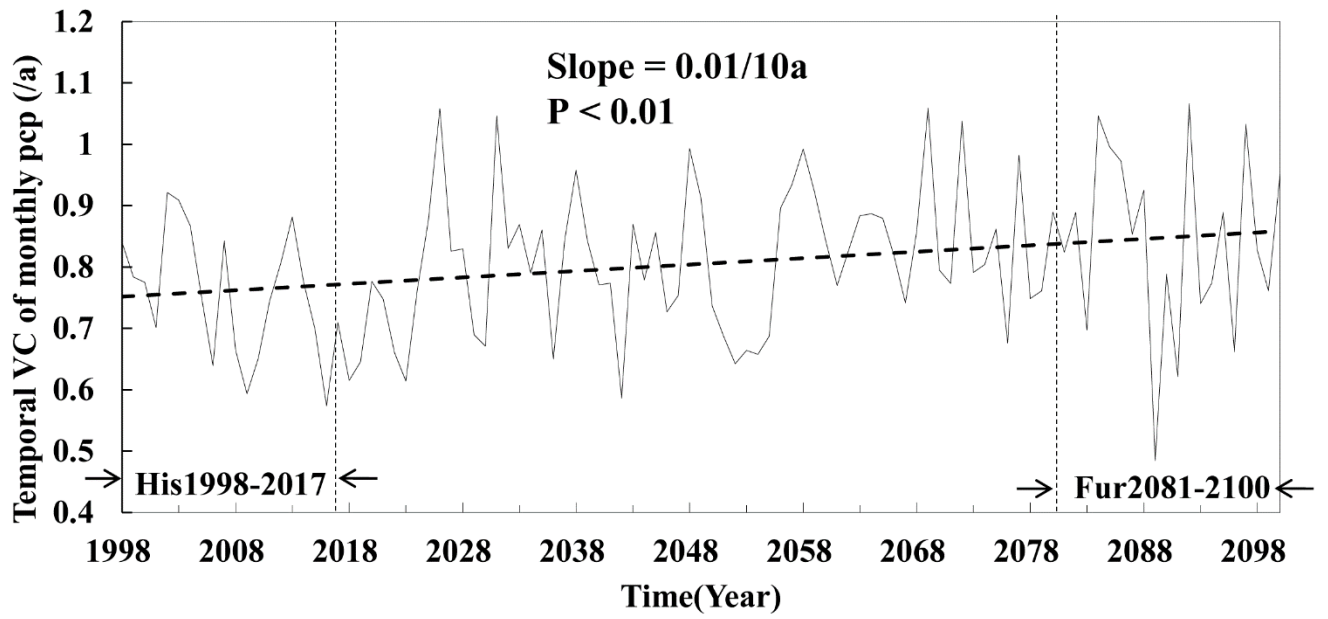




658

659 Fig. 6. The trends of changes in monthly precipitations of extreme wet (EWet) (a) and dry (EDry) (b) months from 1998 to  
 660 2100. The further future period from 2081 to 2100 (Fur2081-2100) and baseline period from 1998 to 2017 (His1998-2017) are  
 661 indicated by arrows. Frequencies of the months in extreme wet (c) or dry (d) months are calculated during the period from  
 662 1998 to 2100.

663

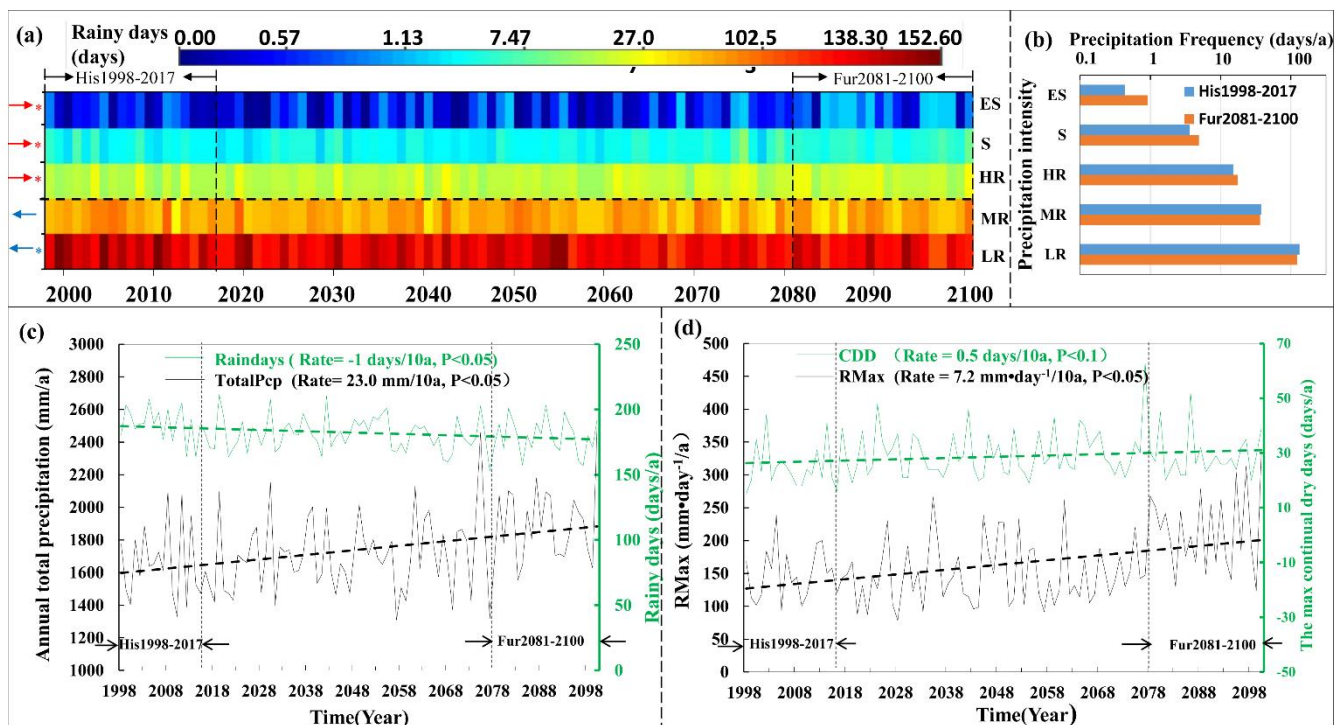


664

665 Fig. 7. The temporal variation coefficients of the extreme month precipitations for each year over 1988 to 2100. The extreme  
 666 months are composed of the extreme wet and dry months. The far future period from 2081 to 2100 (Fur2081-2100) and baseline  
 667 period from 1998 to 2017 (His1998-2017) are indicated by arrows.

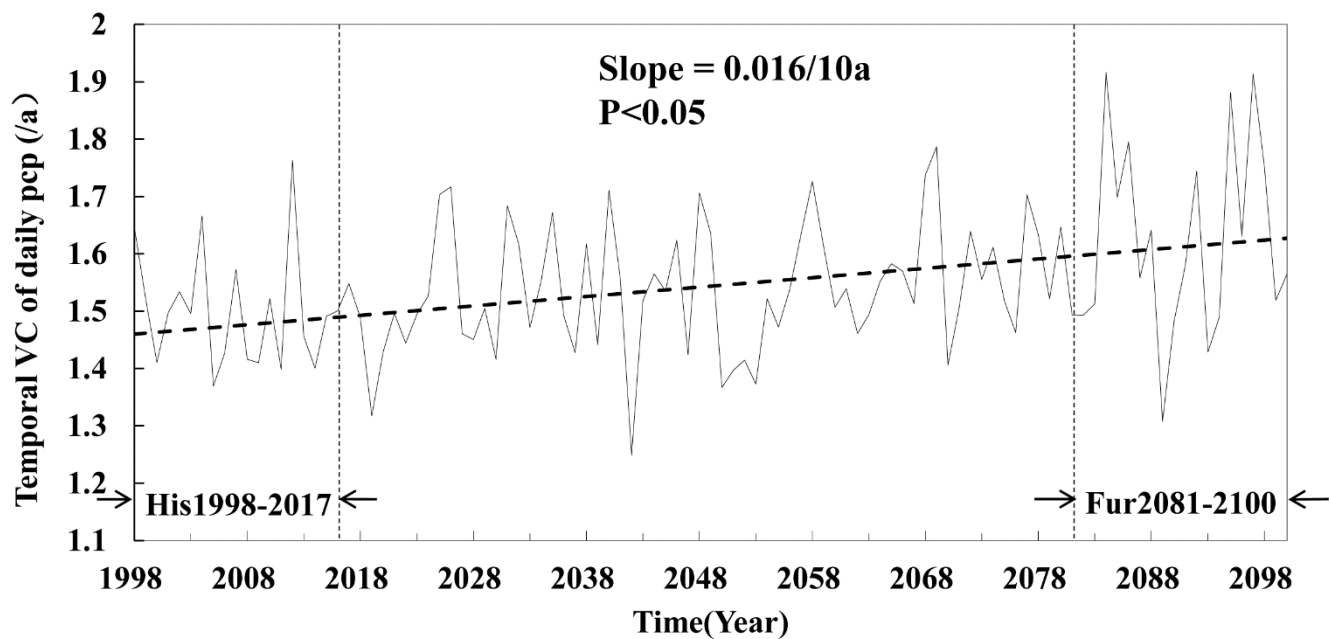
668

669



671

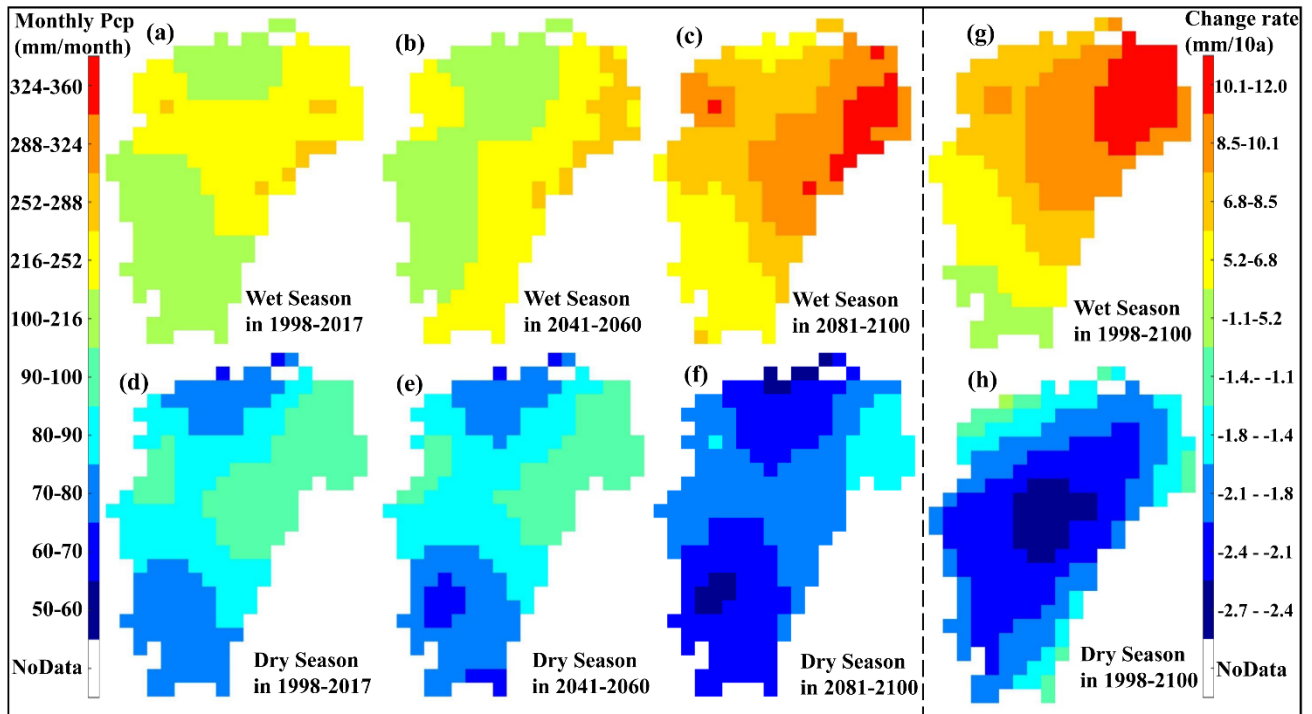
672 Fig. 8. The changes in daily precipitation intensities and frequencies. (a) Precipitation intensities and frequencies for each year  
 673 over 1998 to 2100, where each column represents a year and each row indicates a precipitation intensity. Daily precipitation  
 674 intensities are categorized to 5 classes, Light Rain (LR), Median Rain (MR), Heavy Rain (HR), Rainstorm (S), and Extreme  
 675 Rainstorm (ES) with daily precipitation of 0.1-10, 10-25, 25-50, 50-100 and >100 mm/day, respectively. The moderate rain  
 676 includes LR and MR while the extreme rain is composed of HR, S, and ES. The cell represents an annual frequency of one  
 677 precipitation intensity, with a unit of days. The red (blue) arrows indicate that annual frequency of the precipitation intensity  
 678 experienced an increasing (decreasing) trends over the 103 years (from 1998 to 2100), respectively. The asterisk represents  
 679 the significant trends with  $p < 0.05$ . The far future period from 2081 to 2100 (Fur2081-2100) and baseline period from 1998 to  
 680 2017 (His1998-2017) are indicated by arrows. (b) Precipitation frequencies of LR, MR, HR, S, and ES for Fur2081-2100 and  
 681 His1998-2017, respectively. (c) The change of the long-term data for annual total precipitation (totalPcp) and total rainy days  
 682 (Raindays). (d) The change of the long-term data for annual max daily precipitation (RMax) and annual max continuous dry  
 683 days (CCD).



685

686 Fig. 9. The temporal variation coefficient of daily precipitations for each year over 1988 to 2100. The far future period from  
 687 2081 to 2100 (Fur2081-2100) and baseline period from 1998 to 2017 (His1998-2017) are indicated by arrows.

688



689

690

691

692

693

694

695

696

697

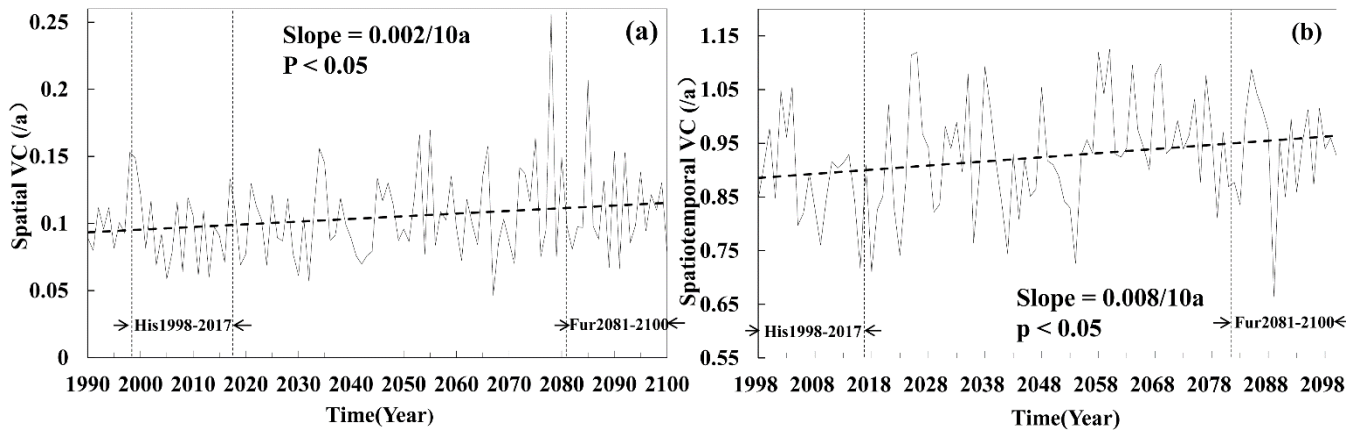
698

699

700

701

Fig. 10. The precipitation changes in the spatial pattern during the period from 1998 to 2100: average monthly precipitations of the wet season (April to July) during the period from 1998 to 2017 (a), 2041 to 2060 (b), and 2081 to 2100 (c); average monthly precipitations of the dry season (December to next February) during the historical period from 1998 to 2017 (d), 2041 to 2060 (e), and 2081 to 2100 (f); change rate of monthly precipitation in wet (g) and dry (h) season from 1998 to 2100. As floods and droughts occur more frequently in extreme months, the precipitation in the analysis considered only the extreme wet (April-July) and dry (September-February) months (Fig. 5c and d). Besides, precipitation is dominated by southeast summer monsoon, which brings water vapor from the sea. The summer monsoon is frequent from the end of spring and start of autumn, covering the wet months April to July. However, though as dry months, the autumn period from September to November is affected by southeast summer monsoon (Tan et al., 1994) slightly because autumns are the transpiration periods of summer to winter. Therefore, winter (December-February) was represented as the dry season with poor rain; while April-July was represented as the wet season with abundant rain.



703

704 Fig. 11. The spatial (a) and spatiotemporal (b) variation coefficient for each year over 1988 to 2100. The further future period

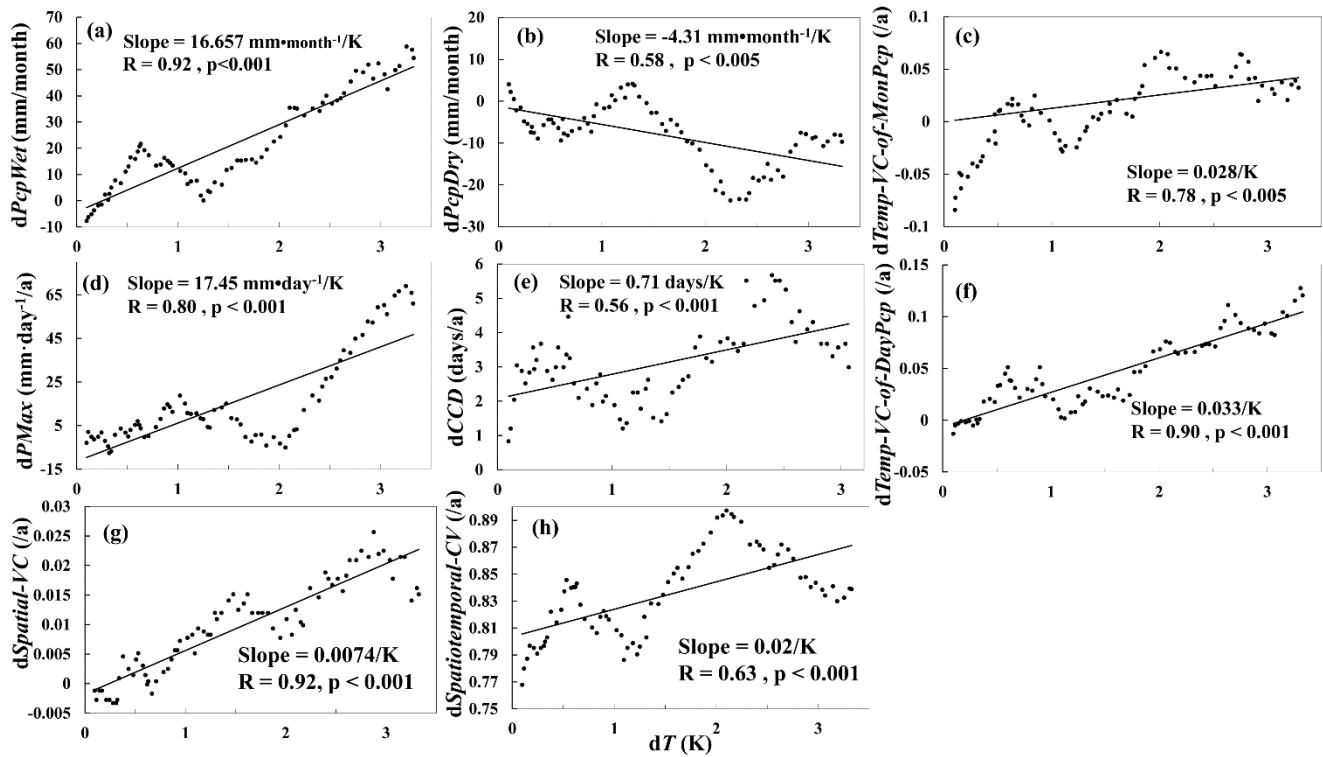
705 from 2081 to 2100 (Fur2081-2100) and baseline period from 1998 to 2017 (His1998-2017) are indicated by arrows.

706

707

708

709



711

712 Fig. 12. The relationship between the precipitation index changes ( $dPcpIndex$ ) and the temperature increment ( $dT$ ). The  
 713 precipitation indexes include annual precipitation in the wet season (PcpWet) (a), annual precipitation in the dry season  
 714 (PcpDry) (b), temporal variance coefficient of monthly precipitations (Temp-VC-of-MonPcp) (c), annual max daily  
 715 precipitation (PMax) (d), annual max continuous dry days (CCD) (e), temporal variance coefficient of daily precipitations  
 716 (Temp-VC-of-DayPcp) (f), spatial variance coefficient (Spatial-VC) (g), and spatiotemporal variance coefficient  
 717 (Spatiotemporal-VC) (h). All the precipitation index changes show significant correlations with temperature increment.

718